



Published in final edited form as:

Cell Rep. 2022 June 14; 39(11): 110937. doi:10.1016/j.celrep.2022.110937.

TRPV6 channel mediates alcohol-induced gut barrier dysfunction and systemic response

Avtar S. Meena^{1,4,5}, Pradeep K. Shukla^{1,4}, Briar Bell^{1,4}, Francesco Giorgianni¹, Rebeca Caires¹, Carlos Fernández-Peña¹, Sarka Beranova¹, Eitaro Aihara², Marshall H. Montrose², Mehdi Chaib¹, Liza Makowski¹, Indira Neeli¹, Marko Z. Radic¹, Valeria Vásquez¹, Jonathan H. Jaggar¹, Julio F. Cordero-Morales^{1,*}, RadhaKrishna Rao^{1,3,6,*}

¹Departments of Physiology, Medicine, Molecular Biology Immunology & Biochemistry, and Pharmaceutical Sciences, University of Tennessee Health Science Center, Memphis, TN 38163, USA

²Department of Pharmacology and Systems Physiology, University of Cincinnati, Cincinnati, OH 45221, USA

³Memphis Veterans Affairs Medical Center, Memphis, TN 38104, USA

⁴These authors contributed equally

⁵Present address: Center for Cellular and Molecular Biology, CSIR, Hyderabad, India

⁶Lead contact

SUMMARY

Intestinal epithelial tight junction disruption is a primary contributing factor in alcohol-associated endotoxemia, systemic inflammation, and multiple organ damage. Ethanol and acetaldehyde disrupt tight junctions by elevating intracellular Ca^{2+} . Here we identify TRPV6, a Ca^{2+} -permeable channel, as responsible for alcohol-induced elevation of intracellular Ca^{2+} , intestinal barrier dysfunction, and systemic inflammation. Ethanol and acetaldehyde elicit TRPV6 ionic currents in Caco-2 cells. Studies in Caco-2 cell monolayers and mouse intestinal organoids show that TRPV6 deficiency or inhibition attenuates ethanol- and acetaldehyde-induced Ca^{2+} influx, tight junction disruption, and barrier dysfunction. Moreover, *Trpv6*^{-/-} mice are resistant to alcohol-induced intestinal barrier dysfunction. Photoaffinity labeling of 3-azibutanol identifies a histidine as a

This is an open access article under the CC BY-NC-ND license (<http://creativecommons.org/licenses/by-nc-nd/4.0/>).

*Correspondence: jcordero@uthsc.edu (J.F.C.-M.), rrao2@uthsc.edu (R.R.).

AUTHOR CONTRIBUTIONS

A.S.M. performed experiments, processed data, and prepared figures; P.K.S. assisted in many of these experiments and processed data; B.B. performed electrophysiology; C.F.-P. conducted intracellular calcium measurements; R.C. performed electrophysiology in Caco-2 cells; F.G. and S.B. performed LC-MS/MS analysis; E.A. conducted some of the initial experiments in enteroids; M.H.M. designed initial enteroid experiments; M.C. and L.M. performed studies in macrophages; I.N. and M.Z.R. performed studies in neutrophils; V.V. contributed to the design of ionic current measurements and manuscript preparation; J.H.J. supervised C.F.-P. in performing intracellular calcium imaging and analyses; J.F.C.-M. was instrumental in designing electrophysiology, preparation and interpretation of data figures, and manuscript writing; R.R. was responsible for the central hypothesis, design, supervision, and execution of the experiments, data interpretation, and manuscript writing.

SUPPLEMENTAL INFORMATION

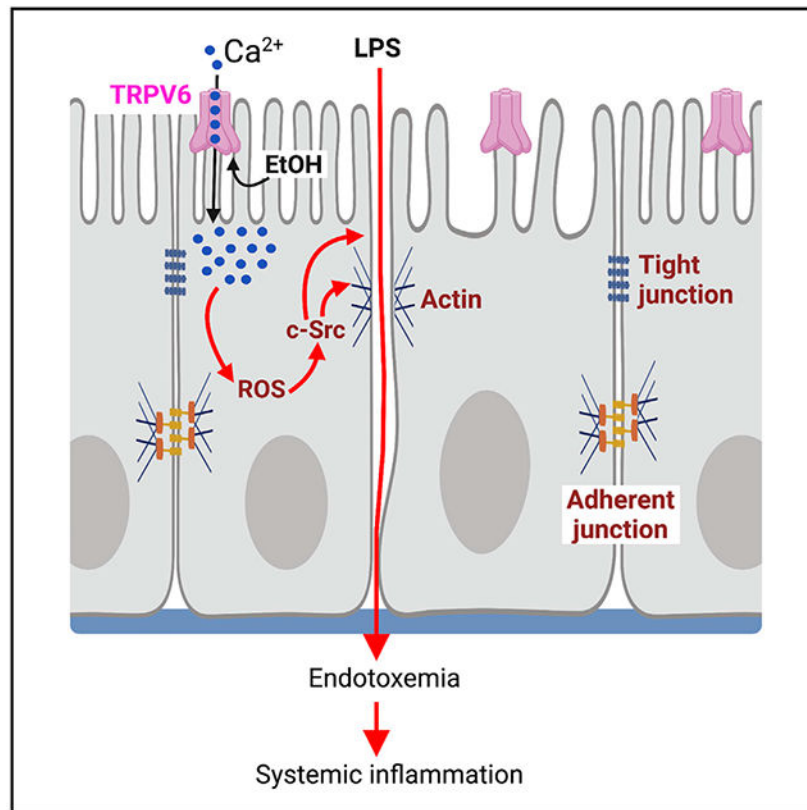
Supplemental information can be found online at <https://doi.org/10.1016/j.celrep.2022.110937>.

DECLARATION OF INTERESTS

The authors declare no competing interests.

potential alcohol-binding site in TRPV6. The substitution of this histidine, and a nearby arginine, reduces ethanol-activated currents. Our findings reveal that TRPV6 is required for alcohol-induced gut barrier dysfunction and inflammation. Molecules that decrease TRPV6 function have the potential to attenuate alcohol-associated tissue injury.

Graphical abstract



In brief

Meena et al. show that the mechanism of alcohol-induced gut permeability, endotoxemia, and systemic inflammation requires the TRPV6 channel. They show that ethanol activates TRPV6, induces calcium influx, and disrupts intestinal epithelial tight junctions. Furthermore, specific histidine and arginine residues at the N terminus fine-tune the alcohol-induced activation of TRPV6.

INTRODUCTION

The common denominator in alcohol-associated disease (AAD) pathogenesis is endotoxemia. The primary mechanism underlying alcohol-associated endotoxemia is gut barrier dysfunction, which causes increased absorption of microbial lipopolysaccharide (LPS) from the intestinal lumen into the systemic circulation (Rao, 2009; Starkel et al., 2018; Vancamelbeke and Vermeire, 2017). LPS induces systemic inflammatory responses and tissue injury in multiple organ systems. Therefore, identifying the initial targets

of ethanol (EtOH) in the intestine is essential to uncovering the mechanisms of AAD pathogenesis.

The primary component of intestinal mucosal barrier function is the epithelial tight junction (TJ). The TJ impedes the diffusion of molecules $>4.0 \text{ \AA}$ in radius, while it exhibits selective permeability to molecules $<4.0 \text{ \AA}$ in radius (Anderson and Van Itallie, 2009; Citi, 2019; Van Itallie and Anderson, 2014). TJ transmembrane proteins include occludin (OCLN), claudins (CLDN), tricellulin, and junctional adhesion molecules (Anderson and Van Itallie, 2009; Citi, 2019). The extracellular domains of transmembrane proteins interact with adjacent cells to form tight cell-cell junctions. The intracellular domains interact with many adapter proteins, such as Zonula occludens-1 (ZO-1), ZO-2, and afadin, which bind to other proteins, including actin-binding proteins. This multiprotein complex is fastened to the actin cytoskeleton (Arnold et al., 2017). The dynamic interactions of signaling molecules with many TJ proteins regulate the barrier function (Gonzalez-Mariscal et al., 2008; Manda et al., 2018; Van Itallie and Anderson, 2018). Evidence indicates that EtOH and its toxic metabolite, acetaldehyde (AA), disrupt intestinal epithelial TJ and barrier function (Rao, 2009). A recent study of Caco-2 cell monolayers, an established model of the intestinal epithelium, demonstrated that EtOH and AA elevate intracellular Ca^{2+} ($[\text{Ca}^{2+}]_i$) and that the Ca^{2+} channel blockers prevent EtOH- and AA-induced TJ disruption (Samak et al., 2016). Depleting extracellular Ca^{2+} from the apical but not basolateral surface of the epithelium inhibits EtOH- and AA-induced TJ disruption and barrier dysfunction, suggesting that Ca^{2+} influx through the apical membrane is involved in EtOH- and AA-induced TJ disruption (Samak et al., 2016).

One of the Ca^{2+} -selective channels on the apical membrane of the rat, mouse, and human intestinal epithelium is the transient receptor potential vanilloid 6 (TRPV6) ion channel (Barley et al., 2001; Peng et al., 2000; Van Cromphaut et al., 2001). TRPV6 is confined to the apical membrane of epithelial cells in multiple organs, including the intestine, pancreas, reproductive organs, brain, and kidney (Wissenbach and Niemeyer, 2007). *TRPV6* deletion in mice resulted in defective intestinal Ca^{2+} absorption, suggesting its primary function in intestinal Ca^{2+} absorption and maintenance of Ca^{2+} homeostasis and bone health (Bianco et al., 2007; Peng et al., 2003a). In the current study, we investigated the role of TRPV6 in alcohol-induced effects on the intestinal epithelium. We found that TRPV6 is required for alcohol-induced intestinal epithelial barrier dysfunction, endotoxemia, and systemic inflammation.

RESULTS

EtOH and AA elicit TRPV6 ionic currents in Caco-2 cell monolayers

Since apical Ca^{2+} influx is required for EtOH- and AA-induced TJ disruption (Samak et al., 2016) and TRPV6 is the primary Ca^{2+} -selective channel in the intestinal epithelium, we asked whether EtOH or AA activates TRPV6 in the intestinal epithelium. Previous studies have shown that TRPV6 elicits inward currents when challenged with EGTA in mammalian cells (Bodding and Flockerzi, 2004; Thyagarajan et al., 2008). Accordingly, we recorded ionic currents in Caco-2 cells after perfusing EGTA, EtOH, AA, or EtOH + AA. Perfusion of cells with 50 mM EtOH alone evoked weak inward currents (13% of

EGTA-elicited currents), while this response was stronger (57% of EGTA-elicited currents) at a concentration of 150 mM (Figures 1A and 1B). AA at a 200 μ M concentration also produced a weak response (34% of EGTA-elicited currents; Figures 1A and 1B). Interestingly, combining EtOH (50 mM) and AA (200 μ M; EtOH + AA) elicited currents greater than the sum of the individual effects (88% of EGTA-elicited currents; Figures 1A and 1B). These data indicate that EtOH and AA synergistically activate TRPV6 in Caco-2 cells. These concentrations of EtOH and AA are physiologically relevant (Ferrier et al., 2006; Guillot et al., 2019). Plasma AA concentrations vary from 40 to 200 μ M after chronic alcohol feeding (Gao et al., 2019; Guillot et al., 2019; Hao et al., 2018; Shimoda et al., 2016), whereas 400–1,000 μ M AA (Han et al., 2019; Pyun et al., 2020) were recorded after acute alcohol administration. SOR-C13, a short peptide based on the amino acid sequence of the protein soricidin, is a specific inhibitor of TRPV6 (Bowen et al., 2013). SOR-C13 abolished the currents elicited by EtOH, AA, and EtOH + AA in Caco-2 cells (Figure 1C). These results provide evidence that EtOH + AA strongly activates TRPV6 in Caco-2 cell monolayers.

TRPV6 mediates the EtOH- and AA-induced rise in Ca^{2+} influx

EtOH + AA-induced TRPV6 currents in the intestinal epithelium suggest that TRPV6 might be involved in EtOH- and AA-induced elevations of Ca^{2+} . To test this hypothesis, we knocked down *Trpv6* expression in Caco-2 cells by transfecting *Trpv6*-specific short hairpin RNA (shRNA) (Figures S1A and S1B). Cells were preloaded with Indo-1, a fluorescent Ca^{2+} indicator, and the 405/485-nm fluorescence ratio was measured to estimate $[\text{Ca}^{2+}]_i$. EtOH + AA rapidly increased $[\text{Ca}^{2+}]_i$ in non-specific RNA (NS-RNA)-transfected cells but not in *Trpv6*-shRNA-transfected cells (Figure 1D), while EtOH or AA alone did not affect $[\text{Ca}^{2+}]_i$. Furthermore, we evaluated the effects of EtOH and AA on Ca^{2+} influx in organoids of the small intestine (enteroids) and colon (colonoids) of wild-type and *Trpv6*^{-/-} mice; organoids are physiologic *in vitro* models of the intestinal epithelium. We observed that EtOH alone caused no effect, but EtOH + AA rapidly increased $[\text{Ca}^{2+}]_i$ in wild-type enteroids and colonoids (Figures 1E and 1F). On the other hand, EtOH + AA failed to increase $[\text{Ca}^{2+}]_i$ in *Trpv6*^{-/-} enteroids or colonoids (Figures 1E and 1F). Recordings of Ca^{2+} changes are presented in Videos S1 and S2. These results indicate that EtOH and AA synergistically increase Ca^{2+} influx in the intestinal epithelium through a TRPV6-dependent mechanism, in line with the EtOH + AA-elicited currents in Caco-2 cell monolayers.

TRPV6 is required for alcohol-induced TJ disruption and barrier dysfunction in the intestinal epithelium

The role of TRPV6 in EtOH + AA-induced Ca^{2+} influx raised the question of its potential involvement in alcohol-induced intestinal epithelial TJ disruption and barrier dysfunction. We evaluated the effect of EtOH + AA on barrier function and TJ integrity in NS-RNA or *Trpv6*-shRNA-transfected Caco-2 cell monolayers. We found that EtOH + AA induces redistribution of OCLN and ZO1 from the epithelial junctions in NS-RNA-transfected, but not *Trpv6*-shRNA-transfected, cell monolayers (Figure 2A). E-Cadherin and β -catenin are major proteins of the epithelial adherens junction (AJ), which is located beneath the TJ (Garcia et al., 2018). AJ is not directly involved in barrier function but indirectly regulates the integrity of TJ (Campbell et al., 2017). EtOH + AA induced redistribution of E-cadherin

and β -catenin in NS-RNA-transfected, but not *Trpv6*-shRNA-transfected, cell monolayers (Figure 2B). EtOH + AA-induced TJ and AJ disruption was associated with decreased transepithelial electrical resistance (TER) (Figure 2C) and increased inulin permeability (Figure 2D). To determine the role of TRPV6 activity in EtOH-induced intestinal barrier dysfunction, we evaluated the effect of SOR-C13 on EtOH + AA-induced TJ disruption and barrier dysfunction in Caco-2 cell monolayers. SOR-C13 attenuated the EtOH + AA-induced redistribution of TJ (Figure 2E) and AJ (Figure 2F) proteins. Additionally, SOR-C13 treatment was associated with a significant attenuation of EtOH + AA-induced decrease in TER (Figure 2G) and increase in inulin permeability (Figure 2H). These results indicate that TRPV6 is required for alcohol-induced TJ and AJ disruption and barrier dysfunction in Caco-2 cell monolayers. The prevention of barrier dysfunction by SOR-C13 confirms the role of TRPV6 activity and indicates the potential application of TRPV6 inhibitors in controlling alcohol-associated tissue injury. To determine the translocation of TJ and AJ proteins to the intracellular compartment in EtOH + AA-treated cell monolayers, we measured intracellular fluorescence for OCLN and E-cadherin. We observed that EtOH + AA significantly increased the intracellular fluorescence for OCLN and E-cadherin, while SOR-C13 blocked these effects (Figures S1C–S1E). This finding indicates that EtOH + AA induces TJ and AJ protein translocation from the junctions to the intracellular compartment.

Previous studies have shown that Src kinase (Basuroy et al., 2003; Elias et al., 2009; Kale et al., 2003; Samak et al., 2011; Sheth et al., 2007) plays a crucial role in the regulation of epithelial TJ integrity. Application of the Src kinase inhibitor blocked EtOH + AA-induced barrier dysfunction in Caco-2 cell monolayers (Samak et al., 2016). Therefore, we examined the potential involvement of TRPV6 and $[Ca^{2+}]_i$ in EtOH + AA-induced c-Src activation by analyzing the levels of c-Src^{P^{Y418}} with immunofluorescence staining. EtOH + AA rapidly increased c-Src activation with peak activation at 15 min (Figures 2I and 2J). The c-Src^{P^{Y418}} fluorescence was localized predominantly at the perijunctional regions of cells and co-localized with the F-actin fluorescence (Figure 2I). EtOH + AA-induced c-Src activation was inhibited by SOR-C13 and BAPTA (a $[Ca^{2+}]_i$ chelator) (Figure 2K). These data indicate that EtOH + AA activates c-Src through a TRPV6- and $[Ca^{2+}]_i$ -dependent mechanism and suggest that Src activity may disrupt the actin cytoskeleton, TJ, and AJ.

TRPV6 is required for alcohol-induced TJ disruption and barrier dysfunction in mouse colonoids

We further explored the involvement of TRPV6 in alcohol-induced intestinal epithelial barrier dysfunction using enteroids and colonoids prepared from wild-type, *Trpv6*^{-/-} and *GFP-Ocln/RFP-ZO1* mice. The data from initial proof-of-concept studies using *GFP-Ocln/RFP-ZO1*-enteroids are presented in Figure S2. Live enteroid fluorescence imaging showed that administering EtOH in the medium induces redistribution of GFP-OCLN and RFP-ZO1 from the epithelial junctions (Figure S2A). Epithelial permeability measured in organoids as the outside-to-inside flux of Alexa Fluor 647 (AF647)-dextran (10 kDa) showed that EtOH increases dextran permeability in a time- and dose-dependent manner (Figures S2B and S2C). Pretreatment with 4-methylpyrazole (4-MP; alcohol dehydrogenase inhibitor), *N*-acetylcysteine (NAC; antioxidant), or diltiazem (DIL; Ca^{2+} channel inhibitor) blocked EtOH-induced dextran permeability (Figures S2D and S2E). Our previous study of Caco-2

cell monolayers showed that EtOH-induced TJ disruption in the intestinal epithelium requires EtOH metabolism into AA by alcohol dehydrogenase (Rao, 2009). EtOH and AA synergistically disrupt TJ through oxidative stress and a Ca^{2+} channel-dependent mechanism (Samak et al., 2016). Our current study confirms these findings in mouse enteroids. However, the EtOH concentration required to disrupt barrier function in this model exceeds the physiologic plasma concentration of 50–150 mM. The disadvantage of this model is that the precise EtOH concentration at the epithelial base is unclear, as the organoids are embedded in Matrigel. Therefore, we used an alternative approach in the following studies by microinjecting EtOH + AA (50 mM + 200 μM , respectively), containing AF647-dextran, into the lumen of *GFP-Ocln/RFP-ZO1* colonoids (colonoids are convenient for microinjection, and the colon is the primary site of LPS absorption).

Time-lapse fluorescence imaging showed that EtOH + AA microinjection increases dextran permeability (inside-to-outside flux) in colonoids in a time-dependent manner (Figure 3A). The initial upward bending followed by a linear time course of dextran permeability suggests that the most significant development of TJ disruption occurred within 1 h; dextran permeability was associated with a collateral redistribution of GFP-OCLN and RFP-ZO1. These results indicate that EtOH and AA disrupt TJ and barrier function in mouse colonoids at physiologically relevant concentrations. In line with our results above, EtOH + AA increased dextran permeability in wild-type, but not *Trpv6*^{-/-}, colonoids (Figure 3B). Immunofluorescence staining of fixed colonoids for OCLN, ZO1, E-cadherin, and β -catenin showed that EtOH + AA induced redistribution of TJ and AJ proteins in wild-type, but not *Trpv6*^{-/-}, colonoids (Figures 3C and 3D). These results indicate that TRPV6 plays an essential role in alcohol-induced TJ and AJ disruption and epithelial permeability in the mouse intestine. In addition, SOR-C13 also inhibited EtOH + AA-induced dextran permeability and redistribution of GFP-OCLN and RFP-ZO1 in mouse colonoids (Figures 3E–3G). These results indicate that TRPV6 activity is required for alcohol-induced TJ and AJ disruption and loss of barrier function in the intestinal epithelium.

***Trpv6*^{-/-} mice are resistant to alcohol-induced colonic TJ disruption, barrier dysfunction, and inflammatory response**

To determine the role of TRPV6 in alcohol-induced disruption of intestinal epithelial junctions and mucosal barrier function *in vivo*, we fed EtOH to wild-type and *Trpv6*^{-/-} mice in a liquid diet for 4 weeks. EtOH-induced changes in body weight, diet intake, colon length, and histopathology are presented in Figure S3. A similar diet intake was maintained in different groups by pair feeding (Figure S3B). While observed in wild-type mice, EtOH-induced changes in body weight and colon length were absent in *Trpv6*^{-/-} mice (Figures S3A and S3C). The cause of weight gain in wild-type mice is unclear, but it is likely due to fat accumulation and a process that involves TRPV6-mediated gut permeability and endotoxemia. Moreover, it is unclear whether the increase in colon length is due to changes in smooth muscle tone or mucosal growth. Histopathology images show that the gross morphology of colonic mucosa was not altered by alcohol feeding in wild-type or *Trpv6*^{-/-} mice (Figure S3G). TRPV6 expression analysis, measuring mRNA and protein levels, indicated that EtOH elevates TRPV6 expression in the wild-type mouse colon (Figures S3D–S3F).

Confocal microscopic examination showed that EtOH induces reduction of OCLN, ZO1, CLDN-3, E-cadherin, and β -catenin at the epithelial junctions in the wild-type, but not *Trpv6*^{-/-}, mouse colon (Figures 4A–4C). TJ disruption was confirmed by a quantitative analysis of the fluorescence at the epithelial junctions (Figures S4A and S4B). Fluorescence densities for OCLN and E-cadherin were significantly reduced by EtOH in wild-type, but not *Trpv6*^{-/-}, mice. Due to their interaction with the actin cytoskeleton, the TJ and AJ proteins are recovered in the actin-rich, detergent-insoluble fractions of the intestinal epithelium (Rao et al., 2002); TJ and AJ disruption results in a reduction of these proteins in the detergent-insoluble fractions. Accordingly, our study shows that EtOH reduces Triton-insoluble fractions of OCLN, ZO-1, CLDN-3, and β -catenin in the colonic mucosa of wild-type, but not *Trpv6*^{-/-}, mice (Figures S4C–S4G). These results indicate that TRPV6 plays an essential role in the mechanism of alcohol-induced disruption of colonic epithelial junctions in mice *in vivo*. To determine the effect of alcohol on TJ and AJ protein expression, we measured mRNA levels for these proteins. Results presented in supplemental information indicate that EtOH decreases mRNA for OCLN, ZO-1, E-cadherin, and β -catenin in wild-type, but not *Trpv6*^{-/-}, mice (Figures S5A–S5D), suggesting that chronic exposure to EtOH results in reduced TJ and AJ protein expression.

EtOH exposure elevated colonic mucosal permeability by several-fold in wild-type, but not *Trpv6*^{-/-}, mice (Figure 4D). Mucosal barrier dysfunction allows absorption of LPS and luminal allergens into the intestinal mucosa, leading to mucosal inflammatory responses. Indeed, EtOH increased the levels of mRNA for *tumor necrosis factor α* (*TNFA*) (Figure 4E), *interleukin-6* (*IL-6*) (Figure 4F), *MCPI* (Figure 4G), *CCL5* (Figure 4H), and *CXCL2* (Figure S5E) in the colonic mucosa; these responses were minimal in EtOH-fed *Trpv6*^{-/-} mice. In addition, the *IL-10* mRNA levels in pair-fed and EtOH-fed *Trpv6*^{-/-} mice were several-fold higher than in pair-fed wild-type mice (Figure S5F). These results indicate that chronic alcohol consumption triggers inflammatory responses in the colonic mucosa primarily through a TRPV6-dependent mechanism.

A previous study showed that EtOH and AA synergistically increases the production of reactive oxygen species (ROS) in Caco-2 cells by a Ca²⁺-dependent mechanism and that antioxidants block EtOH + AA-induced barrier dysfunction (Samak et al., 2016). Similarly, we found that EtOH depletes reduced-protein thiols in the colon, with a collateral elevation of oxidized-protein thiols in wild-type, but not *Trpv6*^{-/-}, mice (Figure 4I). EtOH reduced the level of *Nrf2* mRNA, which encodes a transcription factor regulating antioxidant gene expression, in the wild-type mouse colon (Figure 4J). In contrast, EtOH slightly elevated *Nrf2* mRNA in *Trpv6*^{-/-} mice. The mRNA for the antioxidant genes *SOD2* (Figure 4K), *Trx1* (Figure 4L), *SOD1*, and *Prdx1* (Figures S5G and S5H) were reduced by EtOH in wild-type mice. In *Trpv6*^{-/-} mice, EtOH did reduce *SOD1*, *SOD2*, and *Trx1* mRNA, but their levels still were higher than those in pair-fed wild-type mice. These results suggest that TRPV6-mediated barrier dysfunction and inflammatory responses may be linked to EtOH-induced oxidative stress in the mouse colon *in vivo*. A previous study indicated that oxidative stress-induced activation of c-Src is the likely downstream mechanism linked to TJ disruption (Basuroy et al., 2003). The present study shows that EtOH-induced elevation of activated c-Src (c-Src^{PY418}) in the colonic epithelium is absent in *Trpv6*^{-/-} mice (Figure S6).

TRPV6 is required for alcohol-induced endotoxemia, systemic inflammation, and multiple organ damage

Gut barrier dysfunction contributes to the absorption of LPS from the gut lumen into the systemic circulation, leading to endotoxemia and systemic inflammation (Rao, 2009). Our data show that EtOH elevates plasma LPS (Figure 5A), TNF α (Figure 5B), IL-6 (Figure 5C), and MCP1 (Figure 5D) in wild-type but not *Trpv6*^{-/-} mice, indicating that TRPV6 is required for EtOH-induced endotoxemia and systemic inflammation. Evidence indicates that gut barrier dysfunction and endotoxemia play a crucial role in the pathogenesis of alcohol-associated liver damage (Rao, 2009). The role of TRPV6 in EtOH-induced colonic mucosal permeability and endotoxemia raised the question of its potential role in EtOH-induced liver damage. Remarkably, EtOH failed to elevate plasma alanine transaminase (ALT) (Figure 5E) and aspartate transaminase (AST) (Figure 5F), induce histopathologic changes in liver (Figure 5G), or raise liver triglyceride (Figure 5H) in *Trpv6*^{-/-} mice. Histopathologic examination of the liver from EtOH-fed wild-type mice shows the characteristics of fatty liver, with many pericentral macrovesicular structures representing the lipid droplets. Additionally, hepatocytes with large lipid droplets show the nucleus in a displaced, eccentric position. Such histologic characteristics were absent in *Trpv6*^{-/-} mice. EtOH-induced elevation of *IL-1 β* (Figure 5I), *TNF α* (Figure 5J), and *CXCL1* (Figure 5K) mRNA in the liver was also absent in *Trpv6*^{-/-} mice. Furthermore, EtOH downregulates liver mRNA for antioxidant genes *SOD2* and *Trx1* in wild-type, but not *Trpv6*^{-/-} mice (Figures S7A and S7B). EtOH significantly reduced *Nrf2* mRNA in the liver of wild-type mice (Figure S7C). *Nrf2* mRNA in *Trpv6*^{-/-} mouse liver was substantially lower than in wild-type mice but was not further altered by EtOH. These results indicate that TRPV6 plays a role in alcohol-induced liver damage.

Neuroinflammation is implicated in alcohol-related neuropathology and cognition deficits (Flores-Bastias and Karahanian, 2018; Kane and Drew, 2016; Saito et al., 2016). Evidence suggests that an alteration of the gut-brain axis plays a role in alcohol-induced neuroinflammation. A recent study showed that alcohol increases the expression of TMEM119 (astroglial marker) and GFAP (astrocyte marker) in the brain, indicating the activation of microglia and astrocytes (Shukla et al., 2020). Our data show that EtOH elevates mRNA for proinflammatory *TNF α* (Figure 6A) and *MCP1* (Figure 6B) while reducing the mRNA for anti-inflammatory brain-derived neurotrophic factor (*BDNF*) (Figure 6C) and its receptor, TrkB (Figure 6D), in the cerebral cortex of wild-type, but not *Trpv6*^{-/-}, mice. These results indicate that TRPV6 is also involved in alcohol-induced neuroinflammation.

To determine whether the absence of EtOH-induced systemic inflammation and organ damage in *Trpv6*^{-/-} mice is caused by failure to launch inflammatory responses, we evaluated the innate immune function in macrophages and neutrophils isolated from wild-type and *Trpv6*^{-/-} mice by evaluating their responses to LPS challenge. Our results show that LPS induces similar stimulations of TNF α and IL-6 release in macrophages from wild-type and *Trpv6*^{-/-} mice (Figures S8A and S8B). Functional responses of mature neutrophils in peripheral blood and spleen were examined by measuring ROS production and myeloperoxidase (MPO) release in response to LPS or the Ca²⁺ ionophore A23187.

Neutrophils from both wild-type and *Trpv6*^{-/-} mice released MPO in response to A23187 (Figure S8C); however, the response by neutrophils from *Trpv6*^{-/-} mice was slightly lower compared with neutrophils from wild-type mice. MPO responses to LPS were weak in neutrophils from both wild-type and *Trpv6*^{-/-} mice. LPS and A23187 stimulated ROS production in blood cells from wild-type and *Trpv6*^{-/-} mice (Figure S8D). These data suggest that the lack of EtOH-induced systemic inflammation in *Trpv6*^{-/-} mice is mainly due to the prevention of gut barrier dysfunction and endotoxemia; however, a minor contribution by altered neutrophil function cannot be ruled out.

EtOH and AA elicit ionic currents in TRPV6-expressing HEK 293 cells

To assess the functional interactions between TRPV6 and EtOH or AA, we expressed rat TRPV6 (rTRPV6) in HEK 293 cells and evaluated the effects of EtOH and AA using whole-cell patch-clamp recordings. EtOH perfusion evoked large inward currents of ~80% of the amplitude of EGTA-elicited currents, and AA evoked slightly smaller currents of ~60% of EGTA-elicited currents (Figures 7A–7C). EtOH and AA currents were inhibited by SOR-C13 (Figures S9A–S9C) and did not elicit currents in naive HEK 293 cells (Figures S9D and S9E). Furthermore, neither EtOH nor AA evoked ionic currents in HEK 293 cells expressing rat TRPV1 (rTRPV1; Figures S9F and S9H), suggesting that these organic compounds specifically activate TRPV6. These data raise the question of whether EtOH interacts directly with TRPV6.

Residues in the ankyrin repeat domain fine-tune the TRPV6 response to EtOH

We used photoaffinity binding of 3-azibutanol (a photoactivatable butanol analog) and liquid chromatography with tandem mass spectrometry (LC-MS/MS) analysis to identify potential alcohol-binding sites in TRPV6. Our data show that 3-azibutanol binds to a conserved histidine (H225) in human TRPV6 (hTRPV6) (Figures 7D and S10). H225 is located within the cytosolic ankyrin repeat domain 4 (ARD4) of hTRPV6, which corresponds to the histidine at position 185 (H185) in the rat ortholog (Figure 7D and 7E). Evidence shows that the ARD plays an important role in regulating channel activity (Erler et al., 2004; Phelps et al., 2008; Suzuki et al., 2020). To determine whether H185 plays a functional role in the TRPV6 response to EtOH, we transfected HEK 293 cells with H185A (*rTrpv6*^{H185A}) or wild-type TRPV6 (*rTrpv6*^{WT}) and measured EtOH currents. We found that EtOH-induced currents in *rTRPV6*^{H185A}-expressing cells were significantly lower than in *rTRPV6*^{WT}-expressing cells (Figures 7F, 7G, and 7I). We further tested the impact of a nearby positively charged residue (R134 in the adjacent ARD3; Figure 7E) which could contribute to the TRPV6 EtOH response. We generated an H185/R134 double mutant (*rTRPV6*^{R134A/H185A}) and expressed it in HEK 293 cells. We found that the EtOH-induced currents were further decreased in *rTRPV6*^{R134A/H185A} compared with the *rTRPV6*^{H185A} mutant (Figures 7F, 7H, and 7I). In summary, these results indicate that these amino acids in the ARD fine-tune the TRPV6 response to EtOH.

DISCUSSION

Gut barrier dysfunction is a crucial early step in the pathogenesis of AAD, which includes hepatitis (Sarin et al., 2019; Shasthry, 2020), pancreatitis (Vonlaufen et al., 2007), and

neurodegenerative diseases (Hillemacher et al., 2018). Therefore, identifying molecular targets at the level of gut permeability is essential to describing the pathogenesis of AAD. This study presents evidence for the role of TRPV6 in alcohol-induced gut barrier dysfunction and systemic responses. First, EtOH and AA stimulate inward TRPV6 currents in the apical membranes of the intestinal epithelium. Second, TRPV6 is required for EtOH- and AA-induced elevation of $[Ca^{2+}]_i$ in the intestinal epithelium. Third, EtOH and AA disrupt intestinal epithelial TJ by a TRPV6-dependent mechanism. Fourth, TRPV6 null mice are resistant to alcohol-induced endotoxemia, systemic inflammation, liver damage, and neuroinflammation. Finally, residues in the rTRPV6 ARD (R134 and H185) fine-tune channel EtOH response. Overall, this study identifies TRPV6 as a potential initial target in the pathogenesis of AAD.

EtOH and AA induce barrier dysfunction in Caco-2 cell monolayers by synergistic elevation of $[Ca^{2+}]_i$, Ca^{2+} -mediated oxidative stress, and oxidative stress-mediated TJ disruption (Samak et al., 2016). However, the initial molecular target of EtOH that leads to elevated $[Ca^{2+}]_i$ in the intestinal epithelium is unknown. We show that EtOH and AA synergistically elicit ionic currents in Caco-2 cells. Inhibition of these currents by SOR-C13 indicates that TRPV6, a Ca^{2+} -selective channel, mediates EtOH- and AA-induced ionic currents in Caco-2 cells. The absence of EtOH- and AA-induced elevation of $[Ca^{2+}]_i$ in TRPV6-deficient Caco-2 cells and *Trpv6*^{-/-} intestinal organoids demonstrates that TRPV6 is required for EtOH- and AA-induced Ca^{2+} influx in the intestinal epithelium. The only known function of TRPV6 in the intestinal epithelium to date is Ca^{2+} absorption (Peng et al., 2003b; Pike et al., 2007). Intestinal Ca^{2+} absorption involves Ca^{2+} uptake through the apical membrane and transport across the basolateral membrane into the systemic circulation without elevating the steady state $[Ca^{2+}]_i$. Our data show that alcohol increases $[Ca^{2+}]_i$ through a TRPV6-dependent mechanism. Under normal physiologic conditions, Ca^{2+} binding to calbindin in the cytosol and the feedback inhibition of TRPV6 by $[Ca^{2+}]_i$ are likely mechanisms involved in maintaining low $[Ca^{2+}]_i$ during Ca^{2+} absorption. The precise mechanism of TRPV6-mediated elevation of $[Ca^{2+}]_i$ by EtOH and AA is unclear; alteration of feedback regulation of TRPV6, calbindin binding, and regulation of basolateral Ca^{2+} pumps may be involved. EtOH or AA alone may not disrupt the mechanisms that maintain low basal $[Ca^{2+}]_i$; however, these mechanisms may be compromised by a combination of EtOH and AA.

Our previous study showed that Ca^{2+} influx plays a crucial role in EtOH- and AA-induced TJ disruption in Caco-2 cell monolayers (Samak et al., 2016). The absence of EtOH- and AA-induced TJ disruption in *Trpv6*^{-/-} intestinal organoids and blockade of TJ disruption in wild-type organoids by SOR-C13 indicate that TRPV6-mediated Ca^{2+} influx is required for alcohol-induced intestinal epithelial TJ disruption. This conclusion is further supported by the finding that *Trpv6*^{-/-} mice are resistant to EtOH-induced epithelial TJ disruption and elevation of mucosal permeability *in vivo*. These findings identify TRPV6 as an initial target involved in the mechanism of alcohol-induced gut barrier dysfunction. Furthermore, attenuation of EtOH + AA-induced activation of c-Src in Caco-2 cells by BAPTA and SOR-C13 suggests that TRPV6-mediated Ca^{2+} influx leads to activation of c-Src. The role of TRPV6 in alcohol-induced c-Src activation was confirmed in *Trpv6*^{-/-} mice. Previous

studies have shown that Src kinase plays a crucial role in TJ disruption by inducing tyrosine phosphorylation of TJ proteins (Elias et al., 2009).

Disruption of gut barrier function leads to absorption of endotoxins from the intestinal lumen. Strikingly, our data show that alcohol-induced endotoxemia is absent in *Trpv6*^{-/-} mice. The consequence of endotoxemia is systemic inflammation and multiple organ damage, which raises the question of whether TRPV6 is involved in these systemic responses to alcohol. A failure to elevate plasma cytokines in *Trpv6*^{-/-} mice indicated that TRPV6 is required for this process. The liver is the initial target organ for intestine-derived endotoxins (Enomoto et al., 2000). Thus, endotoxin-mediated inflammatory responses play a crucial role in the pathogenesis of alcohol-associated liver disease (Meroni et al., 2019). The current data show that *Trpv6*^{-/-} mice are resistant to alcohol-induced liver damage, indicating that the TRPV6 channel is required for alcohol-induced liver damage. Furthermore, our data show that TRPV6 deficiency attenuates alcohol-induced inflammatory responses in the cerebral cortex. Thus, TRPV6-mediated activation of the gut permeability-endotoxemia-systemic inflammation pathway is most likely the primary cause of alcohol-induced neuroinflammation. Significant responses to LPS challenge in macrophages and neutrophils isolated from *Trpv6*^{-/-} mice suggest that dysfunctional immune response is not likely a major factor in attenuation of alcohol-induced systemic inflammation.

The synergistic effects of EtOH and AA on the ionic currents in Caco-2 cells suggest that each might have distinct targets that converge to produce a maximal effect. Activation of ionic currents in TRPV6-expressing HEK293 cells by EtOH indicates that it may directly interact with TRPV6. Indeed, 3-azibutanol-binding and LC-MS/MS analyses indicate that H225 is a potential alcohol-binding site in hTRPV6, corresponding to H185 in rTRPV6. The decrease in EtOH activation of rTRPV6 currents by the H185A (located in ARD4) and nearby residue R134A (located in ARD3) mutations indicates that these amino acid residues are required for a complete response to EtOH. Determining the molecular mechanism and conformational changes associated with EtOH binding and activation, as well as AA activity, will require further study.

In summary, this study demonstrates that TRPV6 plays a crucial role in alcohol-induced Ca²⁺ influx in the intestinal epithelium leading to TJ disruption, barrier dysfunction, endotoxemia, systemic inflammation, liver damage, and neuroinflammation. Furthermore, results indicate that a region in the ARD of the TRPV6 channel fine-tunes its EtOH response. These findings identify TRPV6 as an initial target in the mechanism of AAD pathogenesis.

Limitations of the study

In this study, we have used a conventional knockout mouse for TRPV6 deletion. The intestinal epithelial-specific knockout mouse would confirm the role of TRPV6 in the intestinal epithelium in alcohol-induced TJ disruption. Although the present enteroid studies indicate the role of TRPV6 in EtOH- and AA-induced TJ disruption, the *in vivo* studies in tissue-specific knockout would have confirmed the role of gut barrier dysfunction in alcohol-induced liver damage and neuroinflammation. Another limitation is that TRPV6 in the intestinal epithelium is shown to absorb Ca²⁺ from the intestine without altering the

free cytosolic Ca^{2+} . This study shows that alcohol stimulates Ca^{2+} uptake via the TRPV6 channel and increases the cytosolic Ca^{2+} ; however, the mechanism involved is unclear. Further studies are necessary to determine how alcohol stimulates Ca^{2+} absorption through the TRPV6 channel and increases intracellular Ca^{2+} . Furthermore, although EtOH-induced currents were reduced by mutation of R134 and H185, we could not achieve complete attenuation of EtOH-induced TRPV6 channel activity. Further study of the amino acids surrounding the putative interaction site will likely reveal additional residues that play a role in modulating the EtOH-elicited activity of the channel. Moreover, although not supported by our LC-MS/MS analysis, we cannot completely rule out the possibility that another interacting site exists elsewhere on the protein. Considering these limitations in future work could help elucidate more clearly the mechanism of EtOH-mediated TRPV6 activation.

STAR★METHODS

RESOURCE AVAILABILITY

Lead contact—Further information and requests for resources and reagents should be directed to and will be fulfilled by the lead contact, Radhakrishna Rao (rrao2@uthsc.edu).

Materials availability—The plasmids generated in this study are available from the lead contact with the MTA agreements as per institutional requirements.

Data and code availability—Individual values for all graphs are deposited at “figshare” site and are publicly available as of the date of publication. DOI is listed in the key resources table.

Any additional information required to reanalyze the data reported in this paper is available from the lead contact upon request.

EXPERIMENTAL MODELS AND SUBJECT DETAILS

Cell lines

Caco-2 cells: Caco-2_{bbe} cells (ATCC; Rockville, MD, USA) were maintained under standard cell culture conditions in DMEM containing 10% (v/v) fetal bovine serum (Life Technologies, Carlsbad, CA, USA).

HEK 293 cells: HEK 293 cells (ATCC) were cultured in DMEM, supplemented with 10% fetal bovine serum and 1% penicillin-streptomycin at 37°C and 5% CO_2 .

Animals—*Trpv6*^{-/-} mouse strain was a kind gift from Prof. Matthias A. Hediger (University of Bern, Switzerland) received via Dr. Sylvia Christakos (Rutgers New Jersey Medical School, Newark, NJ, USA). *GFP-Ocln/RFP-ZO1* transgenic mice were from Dr. Jerrold Turner (Harvard University, Boston, MA, USA). Adult (8–10 weeks old, male and female) were used for these studies. All animal experiments were approved by the UTHSC Institutional Animal Care and Use Committee.

METHOD DETAILS

Chronic alcohol feeding model—Adult (8–10 weeks old, male and female) *Trpv6*^{-/-} and corresponding wild-type mice were fed a Lieber–DeCarli liquid diet (Dyets Inc., Bethlehem, PA) containing ethanol (a gradual increase from 1% to 6% over four weeks) as described before (Meena et al., 2019). Ethanol was replaced with isocaloric maltose dextrin (Bioserv, Flemington, NJ, USA) in control groups. Diet intake was recorded daily, and body weights were recorded twice a week. Animals were maintained in pairs to facilitate body temperature maintenance and avoid social isolation.

Analysis of 3-Azibutanol binding site in hTRPV6—As previously described by other investigators (Arevalo et al., 2008; Das et al., 2006, 2009), recombinant human TRPV6 (9 µg; Novus Biologicals, Centennial, CO, USA) was incubated with 20 mM 3-Azibutanol in 25 mM Tris buffer (pH 8.0) for 25 min and crosslinked with photoactivation at 365 nm for 45 min at ~1-inch distance. Tryptic digest of protein was then examined by LC-MS/MS analysis for 3-Azibutanol adducts (+72 Da). Proteomics studies were conducted by high-resolution ion mobility tandem mass spectrometer (Synapt G2-*Si*; Waters Corporation) (Kansal et al., 2019; Koirala et al., 2018; Parks et al., 2019). The entire protein content from the sample was extracted with Oasis HLB solid-phase extraction cartridges (Waters) and digested with sequencing grade trypsin (Promega) using established protocols (Kansal et al., 2019). Following digestion, the peptide sample was mixed with a known amount of a tryptic digest of yeast aldehyde dehydrogenase (Waters) as an internal standard for quantification. The sample was analyzed on an Acquity UPLC M-Class nano-LC system (Waters Corporation) interfaced with a Quadrupole Time-of-flight (QToF) tandem mass spectrometer with ion mobility separation (IMS) (Synapt G2-*Si*). The LC-MS/MS system was operated via the MassLynx control software suite (v. 4.1). The raw data were analyzed with Progenesis QI for Proteomics (Nonlinear Dynamics) software. Peptides were identified with the “ion accounting” method from searching a non-redundant, manually curated protein database (Uniprot).

Site directed mutagenesis—Site-directed R134A and H185A mutagenesis in rat *Trpv6* was performed using the QuikChange Lightning Site-Directed Mutagenesis Kit (Agilent), according to the manufacturer’s instructions.

Cell transfection—A vector-based short hairpin RNA (shRNA) method was used to silence TRPV6 gene expression in Caco-2 cells. Targeting sequence was chosen against the nucleotide sequence of human *TRPV6* (GenBank: ECAC2; NM_018646) using Dharmacon siDesigner software. The target sequence was GAAACAGCGCTACACATA (sequence position 467-484). The sequence was further verified by BLAST search of human genome databases and no matches were found other than TRPV6, confirming the uniqueness of this sequence. To construct the shRNA vector, oligonucleotides containing the antisense sequence, hairpin loop region (TTGATATCCG), and sense sequence with cohesive BamHI and HindIII sites were synthesized (Integrated DNA Technologies Inc., Coralville, IA). The corresponding forward and reverse strands were annealed and inserted at BamHI and HindIII sites into the pRNA-Tin-H1.2/Neo (GenScript Corp., Piscataway, NJ) vector, which induces expression of shRNA by the H1.2 promoter and cGFP reporter gene by the CMV

promoter (Promega, WI). The constructs were transformed into DH5 α *E. coli* competent cells for preparation of plasmid DNA. Plasmid DNA were isolated and purified using QIAGEN Plasmid miniprep Kit (Valencia, CA). Insertion of the shRNA sequence was confirmed by releasing it through digestion with BamHI and HindIII.

Trpv6-specific- or the empty vector was transfected (0.3–1.0 μ g of DNA) into Caco-2 cells using Lipofectamine LTX with Plus reagent (ThermoFisher Scientific, Waltham, MA), as described before (Samak et al., 2016). Transfected cells were trypsinized and grown on transwells (6 mm diameter) for four days before exposure to ethanol and acetaldehyde.

Transfections in HEK 293 cells were performed in six-well plates using Lipofectamine 2000 (Thermo Fisher Scientific), according to the manufacturer's instructions. HEK293 cells were co-transfected with *GFP* (200 ng) and 2 mg wild-type (*rTrpv6*^{WT}), H185A mutant (*rTrpv6*^{H185A}), or R134A H185A mutant (*rTrpv6*^{R134A H185A}) rat *Trpv6* gene in a pMO (a pcDNA3.1-based vector with the 5' AND-3' untranslated regions of the beta-globin gene) expression vector.

Patch-clamp electrophysiology

In Caco-2 cells: For whole-cell recordings, the extracellular solution contained 140 mM NaCl, 6 mM KCl, 1 mM MgCl₂, 10 mM glucose, and 10 mM HEPES (pH 7.4). Recording electrode pipettes were made of borosilicate glass (Sutter Instruments) and fire-polished to a resistance between 2.5 and 4 M Ω . Pipettes were filled with an intracellular solution consisting of 140 mM CsCl, 5 mM EGTA, 1 mM MgCl₂, and 10 mM HEPES (pH 7.2). Cells were recorded under voltage-clamp conditions using an Axopatch 200A (Molecular Devices, Union City, CA, USA) using 1s-ramps from –80 to +80 mV, delivered once per second, and a sampling rate of 10 kHz. Currents were analyzed offline using Clampfit v10.4 (Molecular Devices) and plotted using OriginLab software.

In HEK 293 cells: Ionic currents were recorded 36–48 h after transfection, by patch-clamp electrophysiology, with divalent-free intra- and extracellular solutions in the whole-cell configuration, as described above. For experiments with SOR-C13, the inhibitor was included in the intra- and extracellular solutions. The powdered SOR-C13 was initially dissolved in the appropriate solution at a 100 μ M concentration, then applied in a solution containing ethanol or acetaldehyde.

Preparation and growth of organoids—Organoids from the small intestine and colon of mice were prepared as described previously (Mahe et al., 2013). Crypts isolated from the colon, ileum, or jejunum of adult wild-type, *Trpv6*^{-/-}, or *GFP-Ocln/RFP-ZO1* mice were used to grow corresponding organoids. The intestinal segments were flushed with cold Dulbecco phosphate-buffered saline (DPBS; without Ca²⁺ and magnesium), opened longitudinally, and chopped into small pieces. The jejunum and ileum were incubated with 2 mM EDTA in DPBS without Ca²⁺ and Mg²⁺ for 30 min at 4°C, followed by incubation with the dissociation buffer (54.9 mM D-sorbitol and 43.4 mM sucrose in PBS). Crypts were released by gentle shaking for 1–2 min and isolated by filtration through a 70 μ m cell strainer and centrifugation at 2000 \times g. The colon was incubated with an isolation buffer consisting of 500 U/ml collagenase XI, 0.5 U/ml dispase II, 1 mM DTT, and DMEM/F-12

for 30 min at 37°C. Crypts were released from the tissue by passing the solution through an 18G syringe and isolated by filtration and centrifugation. All crypt preparations were embedded in Matrigel (Corning, U.S.A.) at approximately 6 crypts/ml. After polymerization for 15 min at 37°C in a CO₂ incubator, the medium was added. Growth medium consisted of advanced DMEM containing 1X primocin (InvivoGen, San Diego, CA), 10 mM HEPES, 1x N2, 1x B27, 1 mM N-acetylcysteine, 50 ng/mL EGF, 10 mM nicotinamide, 10 nM gastrin, 500 nM A83-01, 10 mM SB202190, 50 ng/mL mHGF, 10 mM 27632, noggin-conditioned medium and R-spondin-conditioned medium. For colonoids, the growth medium was supplemented with a Wnt-conditioned medium. Organoids were passaged 6-8 days after seeding. Experiments were performed between 5-7 days after seeding.

Ethanol and acetaldehyde treatment—Cell monolayers on transwells were incubated in phosphate-buffered saline (PBS) containing 50 mM ethanol and exposed to vapor phase acetaldehyde to achieve a final concentration of 200 μM acetaldehyde as described before (Rao, 1998). In some experiments, cell monolayers were pretreated with 10 μM SOR-C13, custom-synthesized by Peptide 2.0, Inc. (Chantilly, VA, USA), for 30 min before ethanol and acetaldehyde treatment.

For c-Src activation studies, ethanol (50 mM) and acetaldehyde (200 μM, 10 min after ethanol) were administered directly to the incubation medium and incubated at room temperature to avoid acetaldehyde evaporation. At 5-60 min after acetaldehyde treatment, cell monolayers were fixed in 1% paraformaldehyde in PBS (pH 7.4) and stained for F-actin (with AlexFluor 488-phalloidin) and c-Src^{P^Y418} (immunofluorescence method) and imaged by confocal microscopy.

Calcium imaging—Vector or *Tipv6*-shRNA-transfected Caco-2 cells (grown for 36-48 h) and the organoids (grown for 5-7 days) in 60 mm glass-bottom dishes (Nunc™; ThermoFisher Scientific) were used in these assays. Caco-2 cells and organoids were loaded with Indo-1 AM by incubation in calcium buffer medium (135 mM NaCl, 5 mM KCL, 10 mM HEPES, 1mM MgCl₂.6H₂O, 2 mM CaCl₂.2H₂O, and 10 mM glucose, pH 7.4) containing 1 mM Indo-1 AM, 0.04% pluronic F127 and 0.25% DMSO at 37°C for 30 min for Caco-2 cells and 24 h for organoids, in a CO₂ incubator. In these experiments, acetaldehyde (200 μM) was applied directly to the imaging chamber 10 min after ethanol (50 mM) administration. Images were collected at 30s intervals. At the end of the experiment, organoids were exposed to 5 mM ionomycin as a positive control. Two-photon imaging was performed using a Zeiss 710 MP microscope (Zeiss, Jena, Germany) equipped with a water-immersion 20x/1.0 objective and coupled to a Chameleon Vision S tunable laser (Coherent, Palo Alto, CA). Indo-1 was excited at 691 nm (Spectra Database at the University of Arizona, <http://www.spectra.arizona.edu/>), and the emitted fluorescence was collected using two bandpass filters of 380-430 nm (NDD1) and 465-515 nm (NDD2). Cytosolic calcium changes were calculated as the ratio of the emission intensities of NDD1 and NDD2.

Evaluation of epithelial barrier function—Barrier function in the Caco-2 cell monolayers was evaluated by measuring TER and inulin permeability, as described previously (Meena et al., 2019). The basal TER values for Caco-2 cell monolayers were 300-400 Ω x cm². Barrier function in organoids was measured in enteroids and colonoids

from *GFP-Ocln/RFP-ZO1*, *Tipv6^{-/-}*, or wild-type mice, grown on 60 mm glass-bottom dishes (5–7 days), by microinjecting 18.3 nL DPBS containing 50 mM ethanol, 200 μ M acetaldehyde, and AlexaFluor 647-conjugated dextran (AF647-dextran; 10 kDa MW), with or without 10 mM SOR-C13, as described previously (Engevik et al., 2018). Live organoid images were captured for GFP, RFP, and AF647 at 10 and 110 min after microinjection. Outside-to-inside AF647-dextran fluorescence ratio was calculated as an estimate of epithelial permeability. For initial studies (Figure S2), AF647-dextran was added to the medium, and the inside-to-outside fluorescence ratio was calculated.

Gut permeability *in vivo*—Colonic and ileal mucosal permeability was evaluated as described previously (Meena et al., 2019). Mice were injected with FITC-inulin (100 mg/mL solution; 2 μ L/g body weight) via tail vein and the fluorescence in plasma and intestinal flushing was measured after one hour. Fluorescence in the luminal flushing was normalized to fluorescence in corresponding plasma samples and calculated as percent inulin load.

Immunofluorescence microscopy—Immunofluorescence staining, imaging, and measurement of junctional fluorescence were performed as described before (Shukla et al., 2018). Caco-2 cell monolayers and cryosections (10 μ m thick) were fixed in acetone/methanol (1:1) at 0°C for 5 min, permeabilized in 0.2% Triton X-100 in PBS for 10 min, and blocked in 4% non-fat milk in Triton–Tris buffer (150 mM sodium chloride containing 10% Tween-20 and 20 mM Tris, pH 7.4). The organoids were fixed in 3% PFA for 30 min, permeabilized with 0.5% Triton X-100 in PBS for 30 min, and blocked in 5% BSA for two hours. All samples were incubated with primary antibodies (anti-ZO-1, anti-OCN, anti-E-cadherin, anti- β -catenin, and anti-CLDN-3) for one hour at 4°C (24 h for organoids), followed by incubation with the secondary antibodies (goat Alexa Fluor 488-conjugated anti-mouse and anti-rabbit IgG antibodies and Cy3-conjugated anti-mouse and anti-rabbit IgG) for another hour in 4% non-fat milk as described previously (Gangwar et al., 2017). Antibodies were purchased from Invitrogen (Carlsbad, CA), DB Sciences (Billerica, MA), or Molecular Probes (Eugene, OR). Hoechst 33342 dye was administered 10 min before washing and mounting. The fluorescence was visualized in a Zeiss L.S.M. 5 laser scanning confocal microscope, and the images from Z-series sections (1- μ m thickness) were collected using Zeiss L.S.M. 5 Pascal confocal microscopy software (release 3.2). The z-series images were stacked using the software Image J (National Institutes of Health) and processed by Adobe Photoshop (Adobe Systems). Images were captured under identical conditions of laser, gain, and exposure time for each experiment, and they were processed in software using identical levels of brightness and contrasts in each color channel.

Protein thiol assay—Reduced-protein thiols were evaluated by staining cryosections of the colon with BODIPY FL-N-(2-aminoethyl)maleimide (Flm) (Life Technologies, Grand Island, NY, USA) and confocal microscopy at excitation and emission wavelengths of 490 nm and 534 nm, respectively. For measuring oxidized-protein thiols, the reduced-protein thiol was first alkylated with N-ethylmaleimide, followed by the reduction of oxidized protein thiols with tris(2-carboxyethyl)phosphine, before staining with Flm. Control staining was done after N-ethylmaleimide treatment. Fluorescence images were captured using a confocal microscope, and the fluorescence was quantitated with Image J software.

Quantitative RT-PCR—Analysis of specific mRNA by RT-qPCR was performed as described before (Shukla et al., 2018). Total RNA (1.5 µg) was used to generate cDNAs using the ThermoScript RT-PCR system for first-strand synthesis (Invitrogen). Quantitative PCR (qPCR) reactions were performed using cDNA mix (cDNA corresponding to 35 ng RNA) with 300 nmol of primers, in a final volume of 25 µL of 2× concentrated RT2 Real-Time SYBR Green/R.O.X. master mix (Qiagen, Germantown, MD), using an Applied Biosystems QuatStudio 6-Flex Real-Time PCR instrument (Norwalk, CT, USA). The cycle parameters were 50°C for 2 min, one denaturation step at 95°C for 10 min, 40 cycles of denaturation at 95°C for 10s, followed by annealing and elongation at 60°C. The relative gene expression of each transcript was normalized to GAPDH using the Ct method. Sequences of primers used for qPCR are provided in Table S1.

Endotoxin assay—Plasma endotoxin concentrations were measured using Pierce L.A.L. Chromogenic Endotoxin Quantitation Kit (Thermo Scientific, Cat# 88282) according to the vendor's instructions.

Histopathology—Liver and colon tissues were fixed in 10% buffered formalin and 8 µm-thick paraffin-embedded sections were stained with hematoxylin and eosin. Stained sections were imaged in a Nikon 80Ti microscope (Nikon Instruments, Inc., Melville, NY) using a 40× objective lens and a color camera.

Transaminase assay—Plasma alanine transaminase (ALT) (Cayman Chemical, Ann Arbor, MI, USA) and Aspartate transaminase (AST) (BioAssay Systems; Hayward, CA, USA) activities were measured by colorimetric assay according to vendor's instructions.

Triglyceride assay—Liver triglyceride was assayed by the GPO method using the assay kit from Pointe Scientific Inc. (Canton, MI), as described before (Shukla et al., 2018). Lipids were extracted from the tissue by incubation in 3 M potassium hydroxide (in 65% ethanol) for one hour at 70°C followed by overnight at room temperature. Triglycerides were measured by enzymatic hydrolysis into glycerol and free fatty acids, followed by colorimetric measurement of glycerol at a wavelength of 540 nm. Values for hepatic triglycerides were expressed as mg triglyceride/g liver tissue.

Plasma cytokine assay—Plasma cytokine and chemokine were measured with a DuoSet ELISA kit per manufacturer instructions (R&D system, Minneapolis, MN). Briefly, fifty microliters of plasma was incubated in capture antibody-coated microplates overnight, followed by incubation with detection antibody for 2 h. It was then incubated with horseradish peroxidase-conjugated streptavidin for 20 min and with substrate solution for 20 min. The reaction was stopped by stop-solution, and absorbance was measured at 450 nm with wavelength correction at 570 nm.

Immunoblot analysis—Protein lysate from Caco-2 cells transfected with empty vector/TRPV6 shRNA or triton-insoluble colonic tissue fractions were separated by SDS-polyacrylamide gel electrophoresis (7%) and transferred to PVDF membranes as described in a previous study (Basuroy et al., 2003). Membranes were immunoblotted for different proteins using TRPV6, Ca_v1.3, or β-actin antibodies (Invitrogen, Carlsbad,

CA, USA), combined with HRP-conjugated anti-mouse IgG or anti-rabbit IgG secondary antibodies (Sigma-Aldrich, St. Louis, MO, USA). Blots were developed using the ECL chemiluminescence reagent (Pierce, Rockford, IL) and quantitated by densitometry using ImageJ software. The density for each band was normalized to the density of the corresponding actin band.

Preparation of the actin-rich detergent-insoluble fraction—Detergent-insoluble fractions were prepared as described previously (Basuroy et al., 2003). Mucosal scrapping from the colon and ileum were incubated with lysis buffer-CS (Tris buffer containing 1% Triton-X100, 2 µg/mL leupeptin, 10 µg/mL aprotinin, 10 µg/mL bestatin, 10 µg/mL pepstatin-A, 10 µL/mL of protease inhibitor cocktail, 1 mM sodium vanadate, and 1 mM PMSF) and centrifuged at 15,600 x g for 4 min at 4°C to sediment the high-density actin-rich detergent-insoluble fraction. Protein content was measured by the BCA method (Pierce Biotechnology, Rockford, IL). Triton-insoluble and soluble fractions were mixed with an equal volume of 2X concentrated Laemmli's sample buffer, heated at 100°C for 5 min, and 25–40 µg protein samples were used for SDS-polyacrylamide gel electrophoresis followed by immunoblot analysis.

Macrophage isolation and functional analysis—Bone-marrow-derived cells were aseptically collected from wild-type and *Tlr6*^{-/-} mice by spinning down femurs and tibiae before incubation in red blood cell lysis buffer (Gibco) at room temperature for 5 min. Single-cell suspensions were filtered using a 70 µm strainer and were spun down at 300 x g for 5 min. Cells were cultured in RPMI (Gibco) + 10% serum + 50 ng/mL of recombinant mouse m-CSF (Gibco) for 7 days. Fresh media was supplied every 3 days. On day 7, cells were detached using Accutase and re-seeded in an Ultra-low-attachment 6-well plate and were polarized to proinflammatory macrophages using 100 ng/mL LPS (*E. coli*) for an additional 48 h. Supernatants were collected, spun down at 2000 RPM to remove cellular debris, and analyzed for TNFα and IL-6 levels by ELISA.

Neutrophil isolation and myeloperoxidase (MPO) release—Mouse neutrophils were isolated from the spleen using EasySep, mouse Neutrophil Enrichment Kit (Cat# 19762; Stem cell technologies, Cambridge, MA). Cells were seeded in a 48-well plate (200,000 cells/well) in 100 µL of HBSS (10 mM HEPES with calcium and magnesium) with 0.2% rat serum and incubated for 15 min at 37°C. Cells were stimulated by adding an equal volume of 4 µM Ca²⁺ ionophore A23187 (#C7522 Sigma Aldrich). After 4 h incubation, 0.5 U of micrococcal nuclease was added to the wells, swirled, and incubated for 10 min at 37°C. Supernatants were collected and adjusted to 2 mM ethylenediaminetetraacetic acid (EDTA), clarified by centrifugation at 5,000 x g for 5 min, and used for MPO assay. MPO activity was measured by oxidation of tetramethylbenzidine (TMB, 2 mM) in the presence of H₂O₂, followed by spectrophotometry.

Intracellular ROS production in mouse whole blood by DHR-123—Blood was collected by cardiac puncture using heparin as an anticoagulant. Blood (50 µL) was incubated with 5 µL of DHR-123 (5 µg/mL) for 15 min at 37°C. LPS (*Pseudomonas aeruginosa* 10; #L9143, Sigma Aldrich), at a final concentration of (10 µg/mL), A23187 (2

μM), or HBSS was added and incubated for 30 min at 37°C. fMLP (10 nM) was added to the LPS-treated cells and incubated for 15 min. Pelleted cells were suspended in 200 μL of flow buffer, and the samples were analyzed by flow cytometer using forward and side scatter to gate on the PMN population and collecting at least 5000 events in the PMN gate.

QUANTIFICATION AND STATISTICAL ANALYSES

All data are expressed as mean \pm SEM. The differences among multiple groups were first analyzed by ANOVA (Prism 6.0). Tukey's t test was used to determine the statistical significance between multiple testing groups and the corresponding control when a statistical significance was detected. Statistical significance was established at 95% confidence.

Supplementary Material

Refer to Web version on PubMed Central for supplementary material.

ACKNOWLEDGMENTS

We thank Luis O. Romero for his technical expertise. These studies are supported by the Veterans Administration (I01BX003014) and National Institutes of Health grants (R01AA12307, R01DK55532, and R01AA029270) to R.R., as well as R01GM133845 to V.V., R01HL133745, R01HL155180, and R01HL158846 to J.H.J., and R01GM125629 to J.F.C.-M.

REFERENCES

- Anderson JM, and Van Itallie CM (2009). Physiology and function of the tight junction. *Cold Spring Harb. Perspect. Biol* 1, a002584. 10.1101/cshperspect.a002584. [PubMed: 20066090]
- Arevalo E, Shanmugasundararaj S, Wilkemeyer MF, Dou X, Chen S, Charness ME, and Miller KW (2008). An alcohol binding site on the neural cell adhesion molecule L1. *Proc. Natl. Acad. Sci. U S A* 105, 371–375. 10.1073/pnas.0707815105. [PubMed: 18165316]
- Arnold TR, Stephenson RE, and Miller AL (2017). Rho GTPases and actomyosin: partners in regulating epithelial cell-cell junction structure and function. *Exp. Cell Res* 358, 20–30. 10.1016/j.yexcr.2017.03.053. [PubMed: 28363828]
- Barley NF, Howard A, O'Callaghan D, Legon S, and Walters JRF (2001). Epithelial calcium transporter expression in human duodenum. *Am. J. Physiol. Gastrointest. Liver Physiol* 280, G285–G290. 10.1152/ajpgi.2001.280.2.g285. [PubMed: 11208552]
- Basuroy S, Sheth P, Kuppaswamy D, Balasubramanian S, Ray RM, and Rao RK (2003). Expression of kinase-inactive c-Src delays oxidative stress-induced disassembly and accelerates calcium-mediated reassembly of tight junctions in the Caco-2 cell monolayer. *J. Biol. Chem* 278, 11916–11924. 10.1074/jbc.m211710200. [PubMed: 12547828]
- Bianco SD, Peng JB, Takanaga H, Suzuki Y, Crescenzi A, Kos CH, Zhuang L, Freeman MR, Gouveia CH, and Wu J (2007). Marked disturbance of calcium homeostasis in mice with targeted disruption of the Trpv6 calcium channel gene. *J. Bone Miner. Res* 22, 274–285. 10.1359/jbmr.061110. [PubMed: 17129178]
- Bodding M, and Flockerzi V (2004). Ca²⁺ dependence of the Ca²⁺-selective TRPV6 channel. *J. Biol. Chem* 279, 36546–36552. 10.1074/jbc.m404679200. [PubMed: 15184369]
- Bowen CV, DeBay D, Ewart HS, Gallant P, Gormley S, Ilenchuk TT, Iqbal U, Lutes T, Martina M, Mealing G, et al. (2013). In vivo detection of human TRPV6-rich tumors with anti-cancer peptides derived from soricidin. *PLoS One* 8, e58866. 10.1371/journal.pone.0058866. [PubMed: 23554944]
- Campbell HK, Maiers JL, and DeMali KA (2017). Interplay between tight junctions & adherens junctions. *Exp. Cell Res* 358, 39–44. 10.1016/j.yexcr.2017.03.061. [PubMed: 28372972]

- Citi S (2019). The mechanobiology of tight junctions. *Biophys. Rev* 11, 783–793. 10.1007/s12551-019-00582-7. [PubMed: 31586306]
- Das J, Pany S, Rahman GM, and Slater SJ (2009). PKC epsilon has an alcohol-binding site in its second cysteine-rich regulatory domain. *Biochem. J* 421, 405–413. 10.1042/bj20082271. [PubMed: 19432558]
- Das J, Zhou X, and Miller KW (2006). Identification of an alcohol binding site in the first cysteine-rich domain of protein kinase C δ . *Protein Sci.* 15, 2107–2119. 10.1110/ps.062237606. [PubMed: 16943444]
- Elias BC, Suzuki T, Seth A, Giorgianni F, Kale G, Shen L, Turner JR, Naren A, Desiderio DM, and Rao R (2009). Phosphorylation of Tyr-398 and Tyr-402 in occludin prevents its interaction with ZO-1 and destabilizes its assembly at the tight junctions. *J. Biol. Chem* 284, 1559–1569. 10.1074/jbc.m804783200. [PubMed: 19017651]
- Engevik KA, Matthis AL, Montrose MH, and Aihara E (2018). Organoids as a model to study infectious disease. *Methods Mol. Biol* 1734, 71–81. 10.1007/978-1-4939-7604-1_8. [PubMed: 29288448]
- Enomoto N, Ikejima K, Bradford BU, Rivera CA, Kono H, Goto M, Yamashina S, Schemmer P, Kitamura T, Oide H, et al. (2000). Role of Kupffer cells and gut-derived endotoxins in alcoholic liver injury¹. *J. Gastroenterol. Hepatol* 15, D20–D25. 10.1046/j.1440-1746.2000.02179.x. [PubMed: 10759216]
- Erler I, Hirnet D, Wissenbach U, Flockerzi V, and Niemeyer BA (2004). Ca²⁺-selective transient receptor potential V channel architecture and function require a specific ankyrin repeat. *J. Biol. Chem* 279, 34456–34463. 10.1074/jbc.M404778200. [PubMed: 15192090]
- Ferrier L, Berard F, Debrauwer L, Chabo C, Langella P, Bueno L, and Fioramonti J (2006). Impairment of the intestinal barrier by ethanol involves enteric microflora and mast cell activation in rodents. *Am. J. Pathol* 168, 1148–1154. 10.2353/ajpath.2006.050617. [PubMed: 16565490]
- Flores-Bastias O, and Karahanian E (2018). Neuroinflammation produced by heavy alcohol intake is due to loops of interactions between Toll-like 4 and TNF receptors, peroxisome proliferator-activated receptors and the central melanocortin system: a novel hypothesis and new therapeutic avenues. *Neuropharmacology* 128, 401–407. 10.1016/j.neuropharm.2017.11.003. [PubMed: 29113896]
- Gangwar R, Meena AS, Shukla PK, Nagaraja AS, Dorniak PL, Pallikuth S, Waters CM, Sood A, and Rao R (2017). Calcium-mediated oxidative stress: a common mechanism in tight junction disruption by different types of cellular stress. *Biochem. J* 474, 731–749. 10.1042/bcj20160679. [PubMed: 28057718]
- Gao Y, Zhou Z, Ren T, Kim SJ, He Y, Seo W, Guillot A, Ding Y, Wu R, Shao S, et al. (2019). Alcohol inhibits T-cell glucose metabolism and hepatitis in ALDH2-deficient mice and humans: roles of acetaldehyde and glucocorticoids. *Gut* 68, 1311–1322. 10.1136/gutjnl-2018-316221. [PubMed: 30121625]
- Garcia MA, Nelson WJ, and Chavez N (2018). Cell-cell junctions organize structural and signaling networks. *Cold Spring Harb. Perspect. Biol* 10, a029181. 10.1101/cshperspect.a029181. [PubMed: 28600395]
- Gonzalez-Mariscal L, Tapia R, and Chamorro D (2008). Crosstalk of tight junction components with signaling pathways. *Biochim. Biophys. Acta* 1778, 729–756. 10.1016/j.bbamem.2007.08.018. [PubMed: 17950242]
- Guillot A, Ren T, Jourdan T, Pawlosky RJ, Han E, Kim SJ, Zhang L, Koob GF, and Gao B (2019). Targeting liver aldehyde dehydrogenase-2 prevents heavy but not moderate alcohol drinking. *Proc. Natl. Acad. Sci. U. S. A* 116, 25974–25981. 10.1073/pnas.1908137116. [PubMed: 31792171]
- Han H, He Y, Johnson H, Mishra P, Lee H, and Ji C (2019). Protective effects of facilitated removal of blood alcohol and acetaldehyde against liver injury in animal models fed alcohol and anti-HIV drugs. *Alcohol Clin. Exp. Res* 43, acer.14034–1102. 10.1111/acer.14034.
- Hao L, Sun Q, Zhong W, Zhang W, Sun X, and Zhou Z (2018). Mitochondria-targeted ubiquinone (MitoQ) enhances acetaldehyde clearance by reversing alcohol-induced posttranslational modification of aldehyde dehydrogenase 2: a molecular mechanism of protection against alcoholic liver disease. *Redox Biol.* 14, 626–636. 10.1016/j.redox.2017.11.005. [PubMed: 29156373]

- Hillemacher T, Bachmann O, Kahl KG, and Frieling H (2018). Alcohol, microbiome, and their effect on psychiatric disorders. *Prog. Neuro-Psychopharmacol. Biol. Psychiatry* 85, 105–115. 10.1016/j.pnpbp.2018.04.015.
- Kale G, Naren AP, Sheth P, and Rao RK (2003). Tyrosine phosphorylation of occludin attenuates its interactions with ZO-1, ZO-2, and ZO-3. *Biochem. Biophys. Res. Commun* 302, 324–329. 10.1016/s0006-291x(03)00167-0. [PubMed: 12604349]
- Kane CJM, and Drew PD (2016). Inflammatory responses to alcohol in the CNS: nuclear receptors as potential therapeutics for alcohol-induced neuropathologies. *J. Leukoc. Biol* 100, 951–959. 10.1189/jlb.3mr0416-171r. [PubMed: 27462100]
- Kansal R, Richardson N, Neeli I, Khawaja S, Chamberlain D, Ghani M, Ghani QUA, Balazs L, Beranova-Giorgianni S, Giorgianni F, et al. (2019). Sustained B cell depletion by CD19-targeted CAR T cells is a highly effective treatment for murine lupus. *Sci. Transl. Med* 11, eaav1648. 10.1126/scitranslmed.aav1648. [PubMed: 30842314]
- Koirala D, Beranova-Giorgianni S, and Giorgianni F (2018). Data-independent proteome analysis of ARPE-19 cells. *Data Brief* 20, 333–336. 10.1016/j.dib.2018.06.103. [PubMed: 30167441]
- Mahe MM, Aihara E, Schumacher MA, Zavros Y, Montrose MH, Helmrath MA, Sato T, and Shroyer NF (2013). Establishment of gastrointestinal epithelial organoids. *Curr. Protoc. Mouse Biol* 3, 217–240. 10.1002/9780470942390.mo130179. [PubMed: 25105065]
- Manda B, Mir H, Gangwar R, Meena AS, Amin S, Shukla PK, Dalal K, Suzuki T, and Rao RK (2018). Phosphorylation hotspot in the C-terminal domain of occludin regulates the dynamics of epithelial junctional complexes. *J. Cell Sci* 131, jcs206789. 10.1242/jcs.206789. [PubMed: 29507118]
- Meena AS, Shukla PK, Sheth P, and Rao R (2019). EGF receptor plays a role in the mechanism of glutamine-mediated prevention of alcohol-induced gut barrier dysfunction and liver injury. *J. Nutr. Biochem* 64, 128–143. 10.1016/j.jnutbio.2018.10.016. [PubMed: 30502657]
- Meroni M, Longo M, and Dongiovanni P (2019). Alcohol or gut microbiota: who is the guilty? *Int. J. Mol. Sci* 20. 10.3390/ijms20184568.
- Parks C, Giorgianni F, Jones BC, Beranova-Giorgianni S, Moore BM II, and Mulligan MK (2019). Comparison and functional genetic analysis of striatal protein expression among diverse inbred mouse strains. *Front. Mol. Neurosci* 12, 128. 10.3389/fnmol.2019.00128. [PubMed: 31178692]
- Peng JB, Brown EM, and Hediger MA (2003a). Apical entry channels in calcium-transporting epithelia. *News Physiol. Sci* 18, 158–163. 10.1152/nips.01440.2003. [PubMed: 12869616]
- Peng JB, Brown EM, and Hediger MA (2003b). Epithelial Ca²⁺ entry channels: transcellular Ca²⁺ transport and beyond. *J. Physiol* 551, 729–740. 10.1113/jphysiol.2003.043349. [PubMed: 12869611]
- Peng JB, Chen XZ, Berger UV, Weremowicz S, Morton CC, Vassilev PM, Brown EM, and Hediger MA (2000). Human calcium transport protein CaT1. *Biochem. Biophys. Res. Commun* 278, 326–332. 10.1006/bbrc.2000.3716. [PubMed: 11097838]
- Phelps CB, Huang RJ, Lishko PV, Wang RR, and Gaudet R (2008). Structural analyses of the ankyrin repeat domain of TRPV6 and related TRPV ion channels. *Biochemistry* 47, 2476–2484. 10.1021/bi702109w. [PubMed: 18232717]
- Pike JW, Zella LA, Meyer MB, Fretz JA, and Kim S (2007). Molecular actions of 1,25-dihydroxyvitamin D₃ on genes involved in calcium homeostasis. *J. Bone Miner. Res* 22 (Suppl 2), V16–V19. 10.1359/jbmr.07s207. [PubMed: 18290714]
- Pyun CW, Seo TS, Kim DJ, Kim TW, and Bae JS (2020). Protective effects of *Ligularia fischeri* and *Aronia melanocarpa* extracts on alcoholic liver disease (in vitro and in vivo study). *BioMed Res. Int* 2020, 1–11. 10.1155/2020/9720387.
- Rao R (2009). Endotoxemia and gut barrier dysfunction in alcoholic liver disease. *Hepatology* 50, 638–644. 10.1002/hep.23009. [PubMed: 19575462]
- Rao RK (1998). Acetaldehyde-induced increase in paracellular permeability in Caco-2 cell monolayer. *Alcohol Clin. Exp. Res* 22, 1724–1730. 10.1111/j.1530-0277.1998.tb03972.x. [PubMed: 9835287]
- Rao RK, Basuroy S, Rao VU, Karnaky KJ Jr., and Gupta A (2002). Tyrosine phosphorylation and dissociation of occludin-ZO-1 and E-cadherin-beta-catenin complexes from the cytoskeleton by oxidative stress. *Biochem. J* 368, 471–481. 10.1042/bj20011804. [PubMed: 12169098]

- Saito M, Chakraborty G, Hui M, Masiello K, and Saito M (2016). Ethanol-induced neurodegeneration and glial activation in the developing brain. *Brain Sci.* 6, 31. 10.3390/brainsci6030031.
- Samak G, Gangwar R, Meena AS, Rao RG, Shukla PK, Manda B, Narayanan D, Jaggar JH, and Rao R (2016). Calcium channels and oxidative stress mediate a synergistic disruption of tight junctions by ethanol and acetaldehyde in Caco-2 cell monolayers. *Sci. Rep* 6, 38899. 10.1038/srep38899. [PubMed: 27958326]
- Samak G, Narayanan D, Jaggar JH, and Rao R (2011). CaV1.3 channels and intracellular calcium mediate osmotic stress-induced N-terminal c-Jun kinase activation and disruption of tight junctions in Caco-2 CELL MONOLAYERS. *J. Biol. Chem* 286, 30232–30243. 10.1074/jbc.m111.240358. [PubMed: 21737448]
- Sarin SK, Pande A, and Schnabl B (2019). Microbiome as a therapeutic target in alcohol-related liver disease. *J. Hepatol* 70, 260–272. 10.1016/j.jhep.2018.10.019. [PubMed: 30658727]
- Shasthry SM (2020). Fecal microbiota transplantation in alcohol related liver diseases. *Clin. Mol. Hepatol* 26, 294–301. 10.3350/cmh.2020.0057. [PubMed: 32570299]
- Sheth P, Delos Santos N, Seth A, LaRusso NF, and Rao RK (2007). Lipopolysaccharide disrupts tight junctions in cholangiocyte monolayers by a c-Src-TLR4-and LBP-dependent mechanism. *Am. J. Physiol. Gastrointest. Liver Physiol* 293, G308–G318. 10.1152/ajpgi.00582.2006. [PubMed: 17446308]
- Shimoda T, Obase Y, Matsuse H, Asai S, and Iwanaga T (2016). The pathogenesis of alcohol-induced Airflow limitation in acetaldehyde dehydrogenase 2-deficient mice. *Int. Arch. Allergy Immunol* 171, 276–284. 10.1159/000452709. [PubMed: 28049208]
- Shukla PK, Meena AS, Manda B, Gomes-Solecki M, Dietrich P, Dragatsis I, and Rao R (2018). *Lactobacillus plantarum* prevents and mitigates alcohol-induced disruption of colonic epithelial tight junctions, endotoxemia, and liver damage by an EGF receptor-dependent mechanism. *Faseb. J* 32, fj201800351R. 10.1096/fj.201800351r.
- Shukla PK, Meena AS, and Rao R (2020). Prevention and mitigation of alcohol-induced neuroinflammation by *Lactobacillus plantarum* by an EGF receptor-dependent mechanism. *Nutr. Neurosci* 25, 871–883. 10.1080/1028415x.2020.1819105. [PubMed: 32945721]
- Starkel P, Leclercq S, de Timary P, and Schnabl B (2018). Intestinal dysbiosis and permeability: the yin and yang in alcohol dependence and alcoholic liver disease. *Clin. Sci* 132, 199–212. 10.1042/cs20171055.
- Suzuki Y, Sawada H, Tokumasu T, et al. (2020). Novel TRPV6 mutations in the spectrum of transient neonatal hyperparathyroidism. *J. Physiol. Sci* 70, 33. 10.1186/s12576-020-00761-2. [PubMed: 32646367]
- Thyagarajan B, Lukacs V, and Rohacs T (2008). Hydrolysis of phosphatidylinositol 4,5-bisphosphate mediates calcium-induced inactivation of TRPV6 channels. *J. Biol. Chem* 283, 14980–14987. 10.1074/jbc.m704224200. [PubMed: 18390907]
- Van Cromphaut SJ, Dewerchin M, Hoenderop JG, Stockmans I, Van Herck E, Kato S, Bindels RJ, Collen D, Carmeliet P, Bouillon R, and Carmeliet G (2001). Duodenal calcium absorption in vitamin D receptor-knockout mice: functional and molecular aspects. *Proc. Natl. Acad. Sci. U. S. A* 98, 13324–13329. 10.1073/pnas.231474698. [PubMed: 11687634]
- Van Itallie CM, and Anderson JM (2014). Architecture of tight junctions and principles of molecular composition. *Semin. Cell Dev. Biol* 36, 157–165. 10.1016/j.semcdb.2014.08.011. [PubMed: 25171873]
- Van Itallie CM, and Anderson JM (2018). Phosphorylation of tight junction transmembrane proteins: many sites, much to do. *Tissue Barriers* 6, e1382671. 10.1080/21688370.2017.1382671. [PubMed: 29083946]
- Vancamelbeke M, and Vermeire S (2017). The intestinal barrier: a fundamental role in health and disease. *Expert Rev. Gastroenterol. Hepatol* 11, 821–834. 10.1080/17474124.2017.1343143. [PubMed: 28650209]
- Vonlaufen A, Xu Z, Daniel B, Kumar RK, Pirola R, Wilson J, and Apte MV (2007). Bacterial endotoxin: a trigger factor for alcoholic pancreatitis? Evidence from a novel, physiologically relevant animal model. *Gastroenterology* 133, 1293–1303. 10.1053/j.gastro.2007.06.062. [PubMed: 17919500]

Wissenbach U, and Niemeyer BA (2007). Trpv6. *Handb Exp Pharmacol*, 221–234.
10.1007/978-3-540-34891-7_13. [PubMed: 17217060]

Author Manuscript

Author Manuscript

Author Manuscript

Author Manuscript

Highlights

- Ethanol and acetaldehyde elicit inward TRPV6 currents in intestinal epithelial cells
- TRPV6 is required for alcohol-induced barrier dysfunction in the intestinal epithelium
- TRPV6 null mice are resistant to alcohol-induced endotoxemia and systemic inflammation
- H185 and R134 residues in the TRPV6 N terminus fine-tune channel response to ethanol

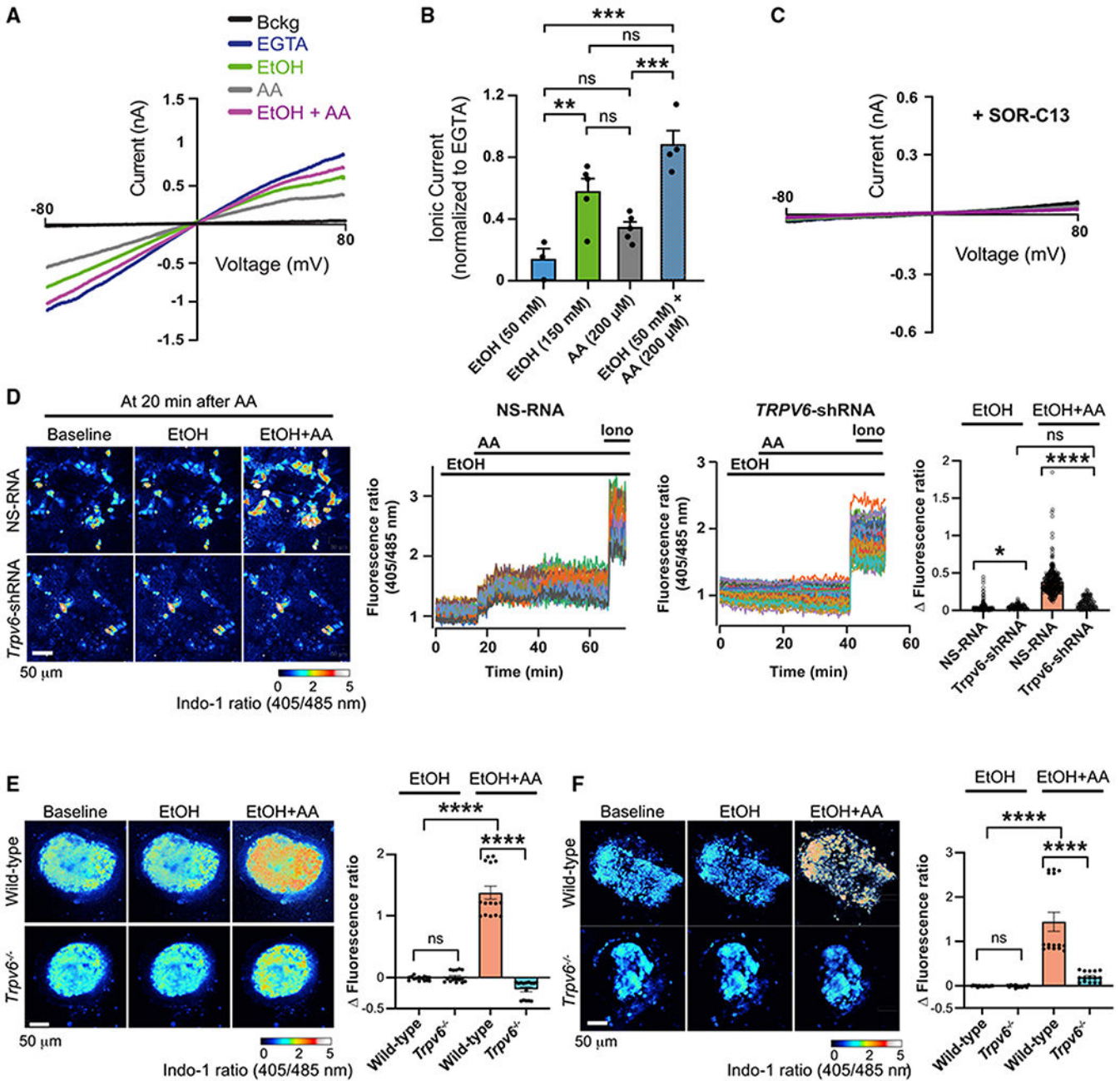


Figure 1. EtOH and AA elicit TRPV6 currents and trigger Ca²⁺ influx in the intestinal epithelium

(A) Representative whole-cell patch-clamp recording from Caco-2 cells challenged with EGTA (2 mM), EtOH (50 or 150 mM), AA (200 μM), or 50 mM EtOH and 200 μM AA (EtOH + AA) combined.

(B) Mean EGTA-normalized currents evoked by EtOH, AA, or EtOH + AA in Caco-2 cells. Values are mean ± SEM (n = 3 for 50 mM EtOH, n = 5 for 150 mM EtOH and 200 μM AA, and n = 4 for EtOH + AA). **p < 0.01 and ***p < 0.005 for significant differences between indicated groups; ns, not significant.

(C) Representative whole-cell patch-clamp recording from Caco-2 cells challenged with EGTA (2 mM), EtOH (50 mM), AA (200 μ M), or EtOH + AA in the presence of SOR-C13 (10 μ M) in the bath and recording pipette. The record is representative of at least five independent patches.

(D) Caco-2 cells were transfected with non-specific RNA (NS-RNA) or *Trpv6*-specific shRNA (see also Figure S1). Intracellular Ca^{2+} ($[\text{Ca}^{2+}]_i$) was measured in transfected cell monolayers using Indo-1 dye and live-cell time-lapse imaging of fluorescence at wavelengths of 405 nm and 485 nm. Cells were treated with EtOH, AA, and ionomycin (Iono). Representative images are presented on the left panel (captured 20 min after AA application). Scale bar, 50 μ m. Real-time changes in 405/485 nm fluorescence ratio are presented in graphs in the middle. The changes in fluorescence ratio from the basal values at 20 min after AA treatment are plotted in the bar graph on the right. Values in the bar graphs are mean \pm SEM (n = 45–50 cells each from six NS-RNA monolayers and four shRNA monolayers). *p < 0.05 and ****p < 0.001 for significant differences between indicated groups; ns, not significant.

(E and F) The effect of EtOH and AA (as above) on $[\text{Ca}^{2+}]_i$ was measured in mouse enteroids (E) and colonoids (F) prepared from wild-type and *Trpv6*^{-/-} mice. Images represent the heatmap images of 405/485 nm ratio measured at 20 min after AA application. Scale bars, 50 μ m. Values in the bar graphs are mean \pm SEM (n = 5 regions each from three different organoids per group). ****p < 0.001 for significant difference between indicated groups; ns, not significant. Real-time video recordings of Ca^{2+} flux in enteroids and colonoids are submitted as Videos S1 and S2.

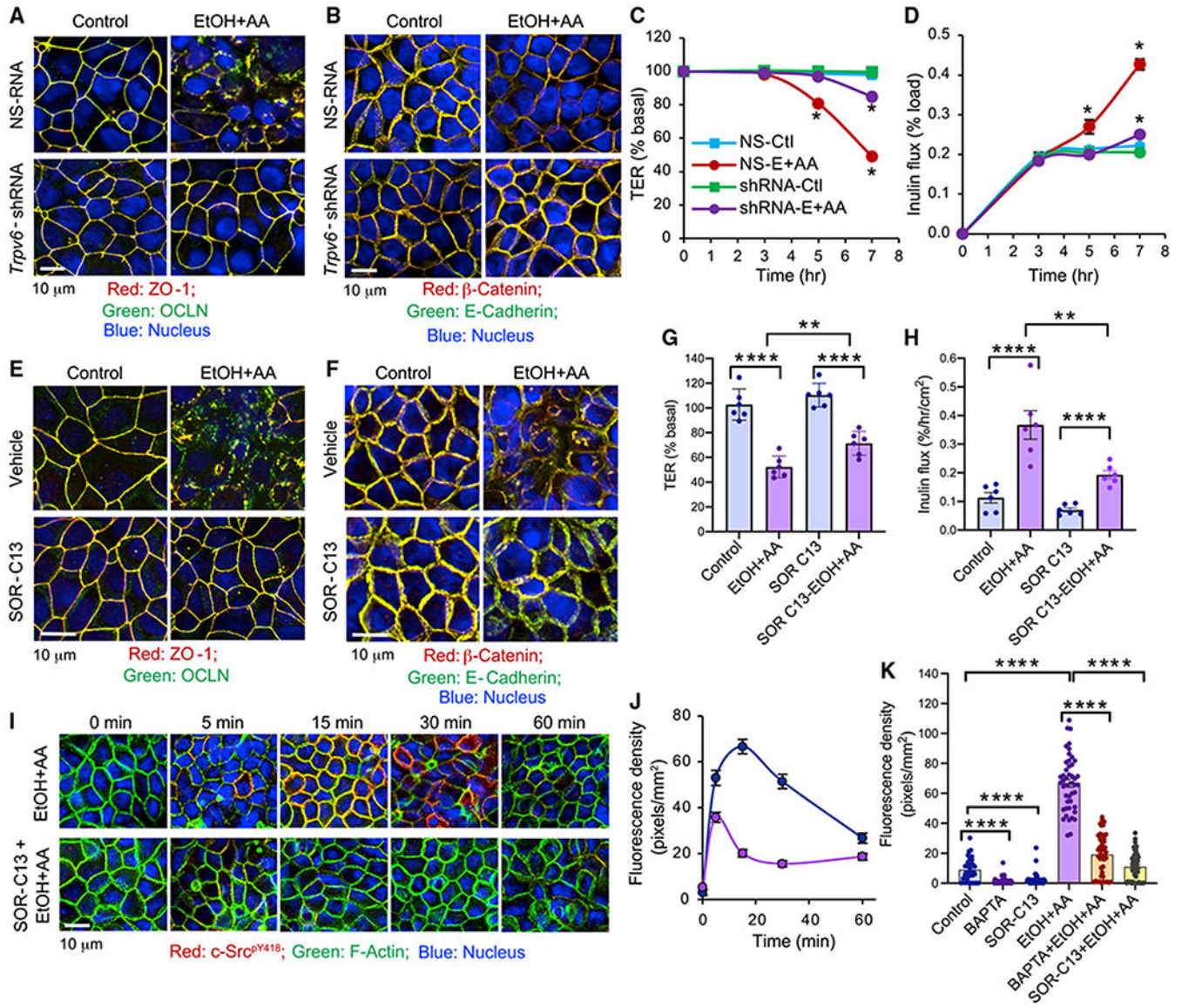


Figure 2. TRPV6 channel plays an essential role in the EtOH and AA-induced disruption of apical junctional complexes and loss of epithelial barrier function in Caco-2 cell monolayers (A–D) Caco-2 cells were transfected with non-specific shRNA (NS-RNA or NS) or *Trpv6*-specific shRNA (*Trpv6*-shRNA or shRNA). Transfected cell monolayers in transwell inserts were incubated with EtOH and AA (EtOH + AA). Cell monolayers were fixed at 7 h of treatment and co-stained for OCLN and ZO-1 (A) or E-cadherin and β -catenin (B). Scale bars, 10 μ m. Transepithelial electrical resistance (TER; C) and transepithelial inulin permeability (D) were measured at varying times. Values are mean \pm SEM (n = 4). *p < 0.05 for significant difference from corresponding control (NS-Ctl or shRNA-Ctl) values. (E–H) Caco-2 cell monolayers were pretreated with or without SOR-C13 for 30 min before incubation with EtOH + AA. After 5 h of EtOH + AA treatment, cell monolayers were fixed and co-stained for OCLN and ZO-1 (E) or E-cadherin and β -catenin (F). Scale bars, 10 μ m. TER (G) and inulin permeability (H) values are mean \pm SEM (n = 6). **p < 0.01 and ****p < 0.0001 for significant differences between indicated groups.

(I–K) Caco-2 cell monolayers were incubated with BAPTA, SOR-C13, or vehicle for 20 min before exposure to EtOH + AA. At varying times after AA administration, fixed cell monolayers were stained for F-actin (green) and c-Src^{pY418} (red; I). Scale bar, 10 μ m. c-Src^{pY418} fluorescence in different cells was quantitated by densitometry (J and K). Values are mean \pm SEM (J: n = 16 cells from two monolayers; K: n = 18 from three monolayers for control and BAPTA groups, n = 26 from four monolayers for the SOR-C13 group, n = 34 from five monolayers for EtOH + AA, with or without BAPTA and SOR-C13). ****p < 0.0001 for significant differences between indicated groups.

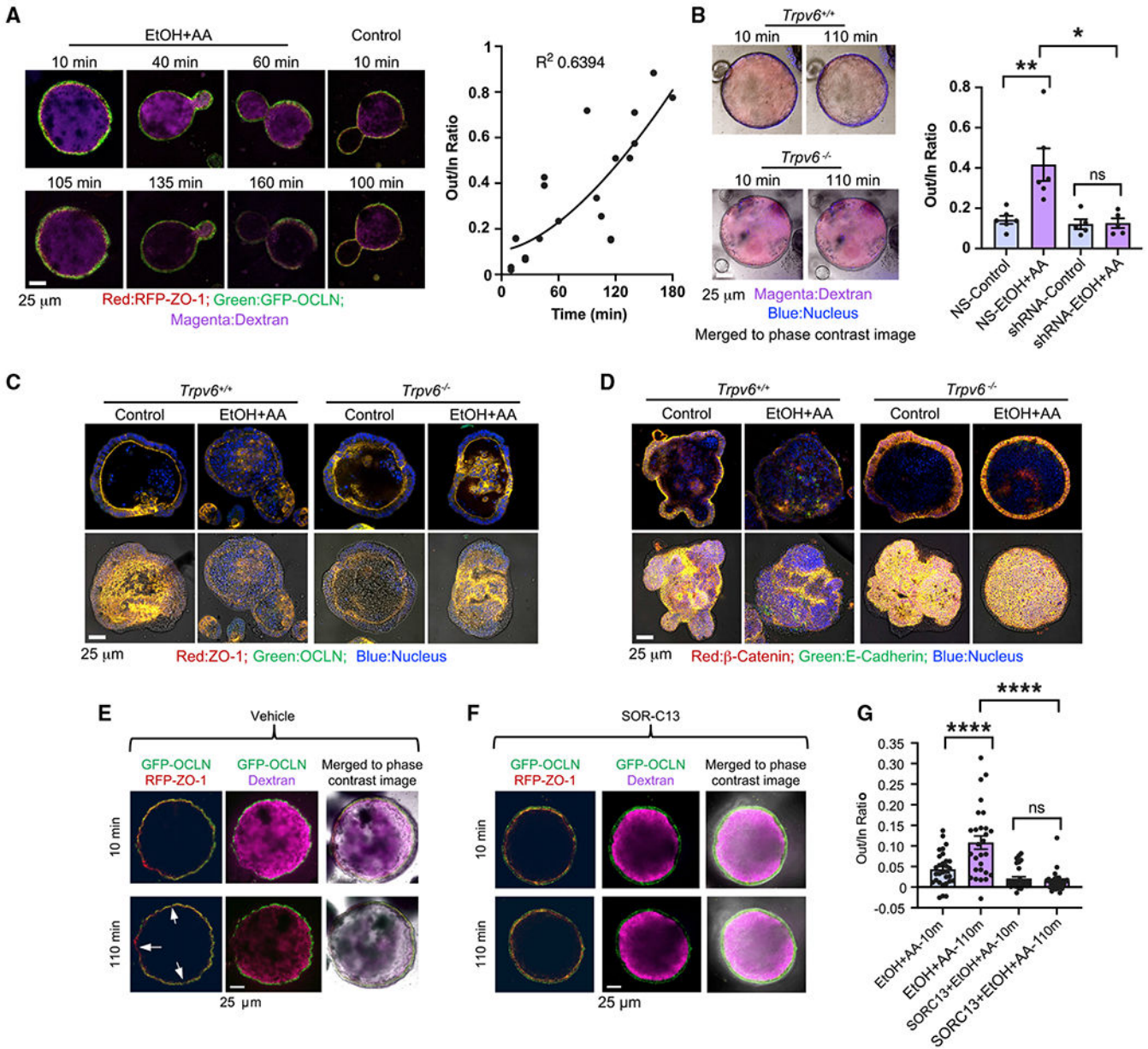


Figure 3. TRPV6 channel plays a role in EtOH and AA-induced TJ disruption and barrier dysfunction in mouse intestinal organoids

(A) *GFP-Ocln/RFP-ZO1* colonoids were microinjected with 50 mM EtOH and 200 μ M AA (EtOH + AA), along with AF647-dextran. Time-lapse fluorescence imaging was performed for GFP, RFP, and AF647, with differential interference contrast microscopy. Representative images captured at indicated times are presented. Scale bar, 25 μ m. The graph shows the outside-to-inside (Out/In) ratio for AF647-dextran fluorescence.

(B) The fluorescence images for the nucleus (Hoechst 33342 dye) and AF647-dextran were evaluated in wild-type and *Trpv6*^{-/-} colonoids at 10 or 110 min after microinjection of EtOH + AA with AF647-dextran as above. Scale bar, 25 μ m. The graph shows the Out/In ratio of AF647-dextran fluorescence measured at 110 min. The values are mean \pm SEM (n = 6

for wild-type and $n = 5$ for *Trpv6*^{-/-} colonoids). * $p < 0.05$ and ** $p < 0.01$ for significant differences between the indicated groups; ns, not significant.

(C and D) Colonoids from wild-type and *Trpv6*^{-/-} mice incubated with 50 mM EtOH and 200 μ M AA (EtOH + AA) in the medium. At 4 h, colonoids were fixed and co-stained for OCLN and ZO-1 (C) or E-cadherin and β -catenin (D). Scale bar, 25 μ m.

(E–G) *GFP-Ocln/RFP-ZO1* colonoids were microinjected with EtOH + AA containing AF647-dextran, with (F) or without (E) 10 μ M SOR-C13. Time-lapse imaging was performed for GFP (green), RFP (red), and AF647 (magenta) at varying times (G); phase-contrast images were captured simultaneously with fluorescence imaging. Arrows in (E) indicate some areas with reduced fluorescence compared with the 10-min image. Scale bar, 25 μ m. The Out/In ratio for AF647-dextran fluorescence was calculated (G). Values are mean \pm SEM ($n = 28$ – 30 regions from three different colonoids).

In (A), (B), and (G), ** $p < 0.01$ and **** $p < 0.001$ for significant differences between the indicated groups; ns, not significant. See also Figure S2.

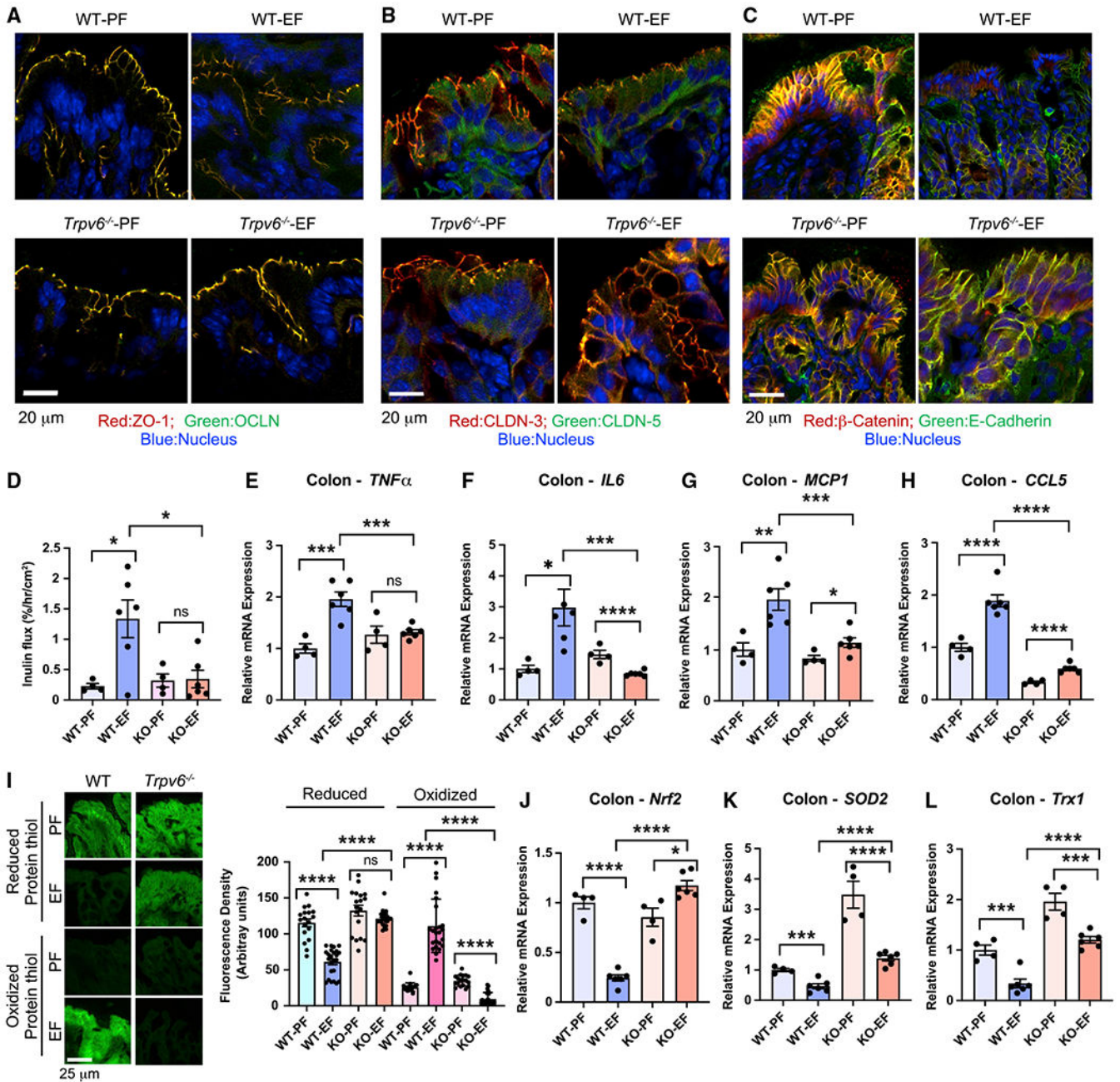


Figure 4. *Trpv6* gene deletion prevents alcohol-induced barrier dysfunction and inflammatory responses in the mouse colon

Adult wild-type (WT) and *Trpv6^{-/-}* (KO) mice were fed a liquid diet with EtOH (EF) or isocaloric maltodextrin (PF), as described in STAR Methods.

(A–C) Cryosections of the colon were fixed and co-stained for OCLN and ZO-1 (A), CLDN-3 and CLDN-5 (B), or E-cadherin and β-catenin (C) by the immunofluorescence method. Scale bars, 20 μm.

(D) Colonic mucosal permeability was evaluated by measuring the vascular-to-luminal flux of FITC-inulin *in vivo*.

(E–H) RNA isolated from the colonic mucosa was analyzed for *TNF α* (E), *IL-6* (F), *MCPI* (G), and *CCL5* (H) mRNA.

(I) Cryosections of the colon were stained for reduced and oxidized-protein thiols. Fluorescence was quantified by densitometric analysis using ImageJ software. Fluorescence from 4–5 different regions was measured in the colonic section from each mouse. Scale bar, 25 μ m.

(J–L) RNA isolated from the colonic mucosa was analyzed for *Nrf2* (J), *SOD2* (K), and *Trx1* (L) mRNA.

Values in all graphs are mean \pm SEM (n = 4 for PF and n = 6 for EF groups). *p < 0.05, **p < 0.01, ***p < 0.005, and ****p < 0.001 for significant differences between the indicated groups; ns, not significant. See also Figures S3–S7.

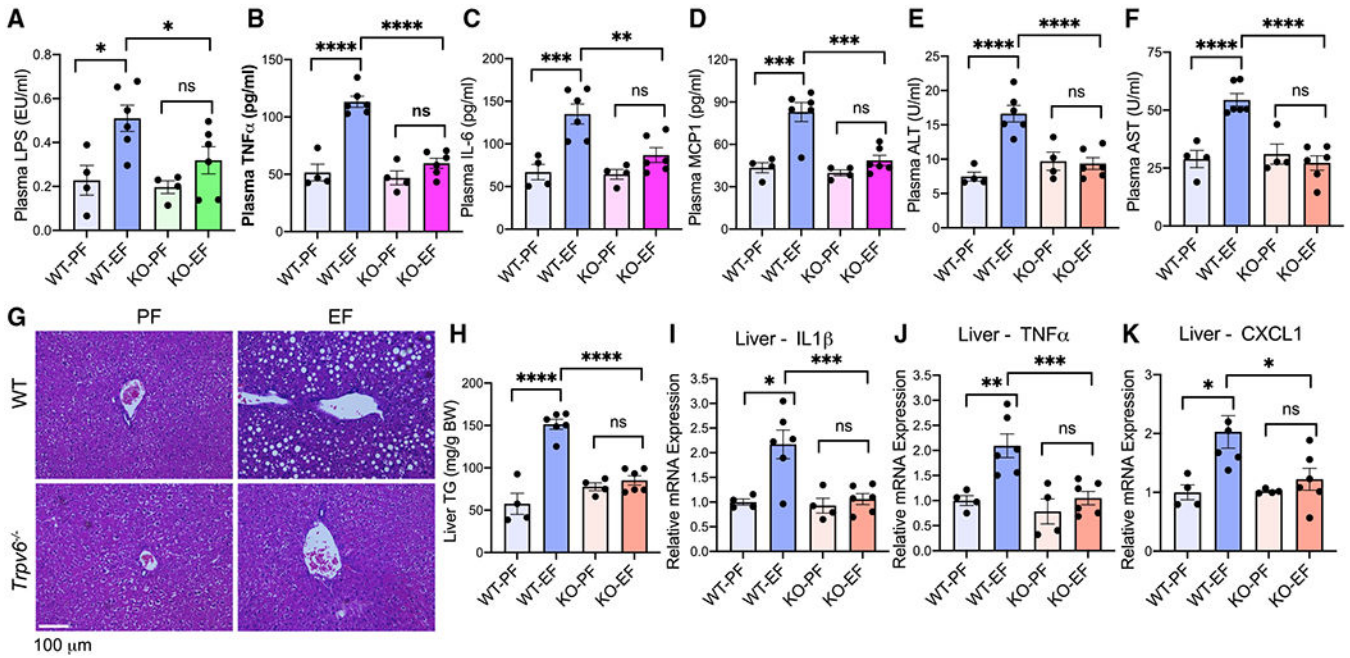


Figure 5. TRPV6 channel is required for EtOH-induced endotoxemia, systemic inflammation, and liver damage

Adult wild-type (WT) and *Trpv6*^{-/-} (KO) mice were fed a liquid diet with EtOH (EF) or isocaloric maltodextrin (PF).

(A) Lipopolysaccharide (LPS) levels were measured in plasma. The values in all graphs are mean \pm SEM (n = 4 for PF and 6 for EF groups); * = p < 0.05 for significant differences between the indicated groups; “ns” = not significant.

(B–D) Plasma levels of TNF α (B), IL-6 (C), and MCP1 (D) were measured by ELISA. The values in all graphs are mean \pm SEM (n = 4 for PF and 6 for EF groups); ** = p < 0.01, *** = p < 0.005, and **** = p < 0.001 for significant differences between the indicated groups; “ns” = not significant.

(E and F) Plasma was analyzed for ALT and AST activity. The values in all graphs are mean \pm SEM (n = 4 for PF and 6 for EF groups); **** = p < 0.001 for significant differences between the indicated groups; “ns” = not significant.

(G) Liver histopathology was performed by H&E staining and bright-field light microscopy. Scale bar = 100 μ m.

(H) Steatosis was assessed by measuring liver triglyceride content. The values in all graphs are mean \pm SEM (n = 4 for PF and 6 for EF groups); **** = p < 0.001 for significant differences between the indicated groups; “ns” = not significant.

(I–K) Inflammatory responses in the liver were determined by measuring mRNA for *IL-1 β* (I), *TNF α* (J), and *CXCL1* (K). The values in all graphs are mean \pm SEM (n = 4 for PF and 6 for EF groups); * = p < 0.05, ** = p < 0.01, *** = p < 0.005, and **** = p < 0.001 for significant differences between the indicated groups; “ns” = not significant.

See also Figure S8.

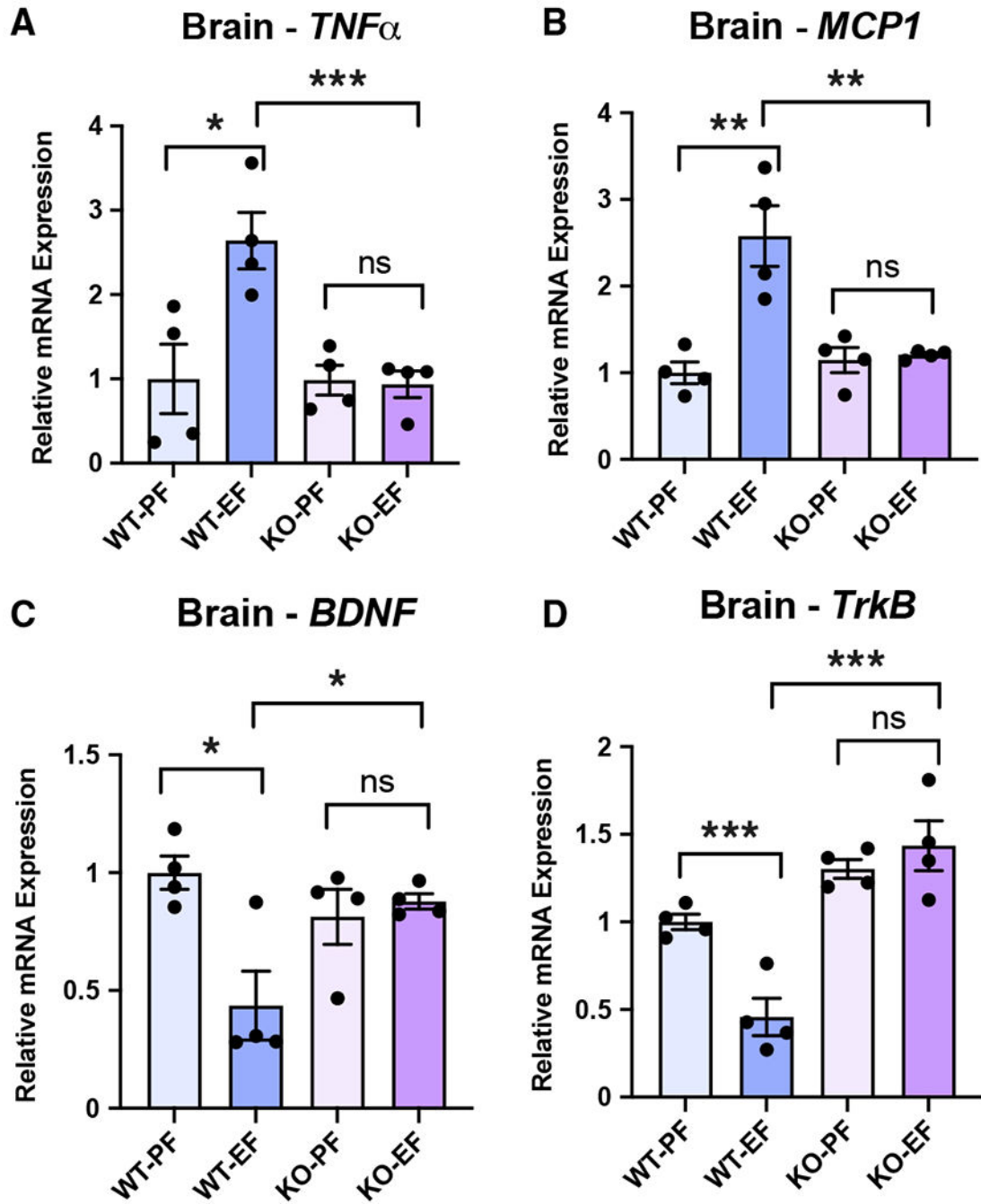


Figure 6. TRPV6 channel is required for EtOH-induced neuroinflammation

(A–D) Adult wild-type (WT) and *Trpv6*^{-/-} (KO) mice were fed a liquid diet with EtOH (EF) or isocaloric maltodextrin (PF). Neuroinflammation was evaluated by measuring mRNA for *TNF α* (A), *MCP1* (B), *Bdnf* (C), and *TrkB* (D) in the cerebral cortex. In all graphs, the values are mean \pm SEM (n = 4 for PF and n = 6 for EF groups). *p < 0.05, **p < 0.01, and ***p < 0.005 for significant differences between the indicated groups; ns, not significant.

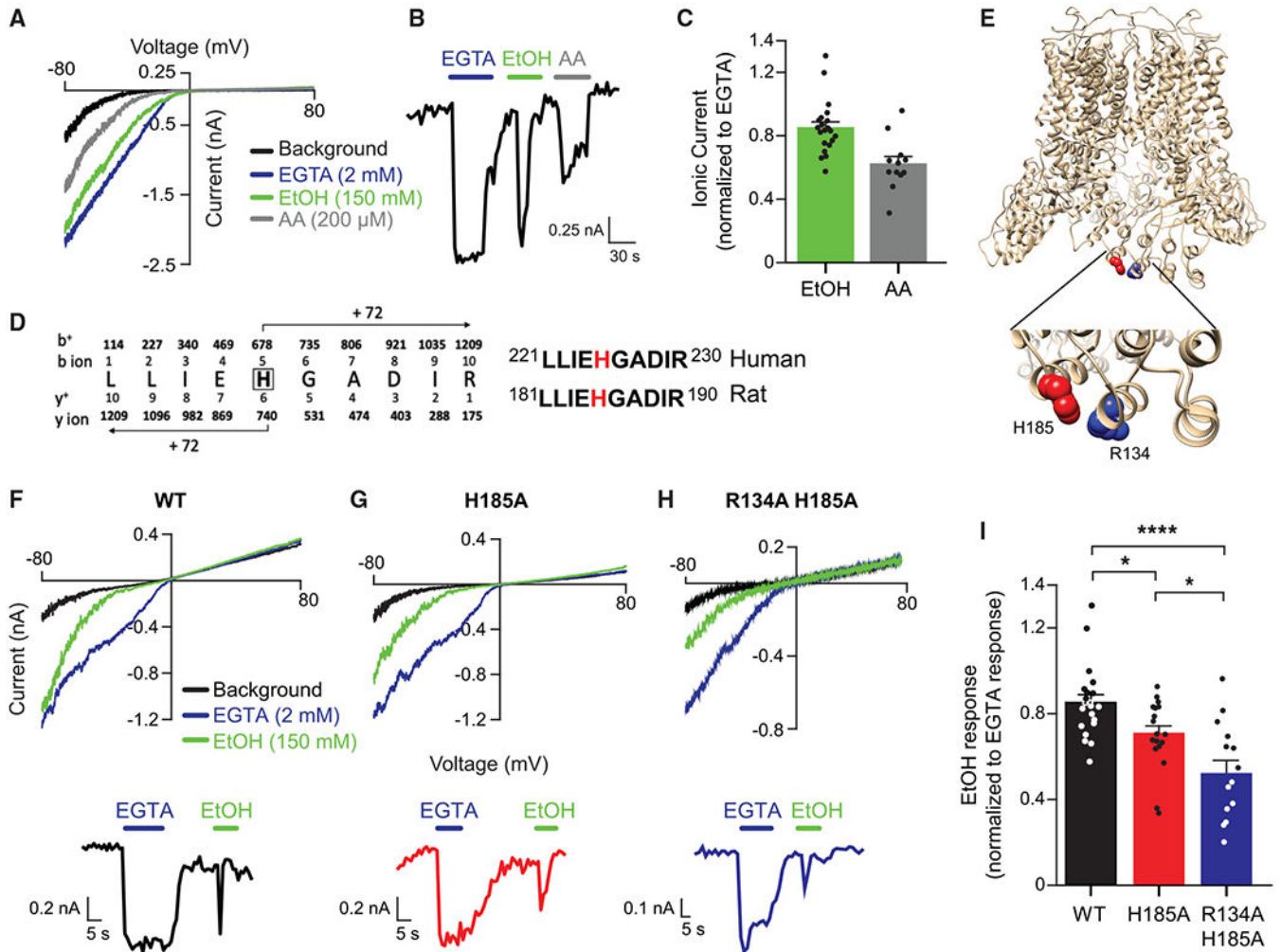


Figure 7. Mutations in the ARD of rat TRPV6 diminish EtOH-activated currents

(A) Representative whole-cell patch-clamp recording (-80 to $+80$ mV voltage-ramps) from rat TRPV6-expressing HEK293 cells challenged with EGTA (2 mM), EtOH (150 mM), and AA (200 μ M).

(B) Time course of the currents at -80 mV, extracted from the record shown in (A).

(C) Mean EGTA-normalized currents evoked by EtOH or AA ($n = 21$ and 12 , respectively).

(D) Sequence alignment of a conserved region of human and rat TRPV6. The putative EtOH-interacting histidine (highlighted in red) was identified by 3-azibutanol binding and mass spectrometry, as shown in Figure S10.

(E) Ribbon representation of rTRPV6 (PDB: 6BOB). The histidine residue indicated in (D) (red, H185) and a nearby arginine residue (blue, R134) are shown as spheres (inset).

(F–H) Top: representative whole-cell patch-clamp recordings from HEK293 cells expressing wild-type (WT), H185A, or R134A H185A mutant rat TRPV6 challenged with 150 mM EtOH or 2 mM EGTA. Bottom: time course of the currents at -80 mV for WT (black), H185A (red), or R134A H185A (blue) mutant TRPV6, extracted from the records shown in the respective upper panels.

(I) EGTA-normalized currents evoked by EtOH in WT, H185A, and R134A H185A mutant rat TRPV6 (n = 21, 19, and 13, respectively). *p < 0.05, ****p < 0.0001. See also Figure S9.

Author Manuscript

Author Manuscript

Author Manuscript

Author Manuscript

KEY RESOURCES TABLE

REAGENT or RESOURCE	SOURCE	IDENTIFIER
Antibodies		
Occludin	Invitrogen	71-1500; RRID: AB_2533977
ZO-1	Invitrogen	40-2200; RRID: AB_2533456
E-cadherin	ThermoFisher	14-3249-82; RRID: AB_1210458
β -Catenin	Invitrogen	PA5-77934; RRID: AB_2735522
c-Src ^{pY418}	MyBiosource	190090
AlexaFluor 488-mouse IgG	ThermoFisher	A-11001
FITC-mouse anti-occludin	Invitrogen	33-1511; RRID: AB_87042
Cy3-rabbit IgG	Millipore Sigma	AP106C; RRID: AB_92245
HRP-mouse IgG	Millipore Sigma	AP127P; RRID: AB_92472
HRP-rabbit IgG	Millipore Sigma	12-348; RRID: AB_390191
Claudin-3	Invitrogen	PA5-32353; RRID: AB_2549824
Claudin-5	Invitrogen	35-2500; RRID: AB_2533200
Trpv6	Origene	TA590262
Ca _v 1.3	Origene	TA326516
β -Actin	Millipore Sigma	A2228; RRID: AB_476697
Chemicals, peptides, and recombinant proteins		
Sodium Chloride	Fisher Scientific	S271-500
Potassium Chloride	Fisher Scientific	P217-500
Magnesium Chloride	Fisher Scientific	BP214-500
Glucose	Sigma	G8270-1KG
HEPES	Fisher Scientific	BP310-100
Hydrochloric Acid	Fisher Scientific	A144-212
Sodium Hydroxide	Fisher Scientific	SS266-1
Cesium Chloride	Acros	7647-17-8
Cesium Hydroxide	Acros	35103-79-8
EGTA	Fisher Scientific	O2783-100
Lipofectamine 2000	Invitrogen	52887
Opti-MEM	Gibco	31985-070
DMEM	Gibco	11965-092
Fetal Bovine Serum	Gibco	10082-147
Penicillin-Streptomycin	Sigma	P4333-100
Ethanol	Fisher Scientific	BP2818-500
Acetaldehyde	Millipore Sigma	75-07-0
SOR-C13	Peptide 2.0 Inc.	Custom synthesis
BAPTA-AM	Millipore Sigma	126150-97-8
Indo-1 AM	ThermoFisher	I1223
AlexaFluor 488-phalloidin	Invitrogen	A12379

REAGENT or RESOURCE	SOURCE	IDENTIFIER
Hoechst 33342	Invitrogen	H3570
AlexaFluor 647-dextran	Invitrogen	D22914
pRNATin-H1.2/Neo	Genscript Corp	SD1223
FITC-inulin	Millipore Sigma	F3272
4-Methylpyrazole	Millipore Sigma	56010-88-9
N-Acetylcysteine	Millipore Sigma	A7250
Diltiazem	Millipore Sigma	D2521
Lipopolysaccharide (<i>P. aeruginosa</i>)	Millipore Sigma	L9143
Lieber-DeCarli diet	Dyets Inc.	710260
Maltose dextrin	BioServe	3650
3,3-Azo-1-butanol	Santa Cruz Biotech	25055-82-7
Trypsin	Promega	V5111
Peptide extraction cartridge	Waters	WAT094225
Lipofectamine LTX	ThermoFisher	A12621
Lipofectamine 2000	ThermoFisher	11668027
Transwells	Millipore Sigma	CLS3460
Collagenase XI	Millipore Sigma	C7657
Dispase II	Millipore Sigma	D4693
Triton X100	Millipore Sigma	T8787
Leupeptin	Millipore Sigma	103476-89-7
Pepstatin-A	Millipore Sigma	26305-03-3
Aprotinin	Millipore Sigma	A1250000
Bestatin	Millipore Sigma	65391-42-6
Dithiothreitol	Millipore Sigma	16096-97-2
Nicotinamide	Millipore Sigma	1090-61-7
Matrigel	Millipore Sigma	CLS354277
Primocin	InvivoGen	amt-pm-1
Gastrin	Millipore Sigma	G9145
SB202190	Millipore Sigma	S7067
hHGF	R&D Systems	2207
R-spondin conditioned medium	Laboratory of Radhakrishna Rao	N/A
Noggin conditioned medium	Laboratory of Radhakrishna Rao	N/A
Wnt conditioned medium	Laboratory of Radhakrishna Rao	N/A
Paraformaldehyde	Millipore Sigma	30525-89-4
Pluronic F127	ThermoFisher	P3000MP
BODIPY FL-N-(2 aminoethyl)maleimide Pierce-N-Ethylmaleimide	ThermoFisher	B10250
ECL chemiluminescence reagent	ThermoFisher	34095
RBC lysis buffer	BioLegend	420301
m-CSF	ThermoFisher	PHC9504
Accutase	Millipore Sigma	A6964
LPS (<i>E. coli</i>)	Millipore Sigma	L4391
A23187	Millipore Sigma	C7522

REAGENT or RESOURCE	SOURCE	IDENTIFIER
Tetramethyl benzidine	Millipore Sigma	T0440
Hydrogen peroxide	Millipore Sigma	7722-84-1
iMLP	Millipore Sigma	59880-97-6
Critical commercial assays		
QuikChange Lightning Site-Directed Mutagenesis Kit	Agilent	210519-5
RT-qPCR kit	Bio Rad	12012901
Duoset ELISA kit	R&D Systems	DY008
LPS assay kit	ThermoFisher	88282
AST assay kit	Cayman chemical	701640
ALT assay kit	Cayman chemical	700260
Triglyceride assay kit	Pointe Scientific	T7532120
EasySep cell isolation kit	Stem cell technologies	19762
Experimental models: Cell lines and transgenic mice		
Human: Caco-2 _{bbe}	ATCC	CRL-2102
Human: HEK293	ATCC	CRL-1573
<i>Trpv6</i> ^{-/-} mice		N/A
<i>GFP-Ocln/RFP-ZO1</i> mice		N/A
Oligonucleotides		
See Table S1 for oligonucleotide information		
Recombinant DNA		
Plasmid: <i>TRPV6</i> pMO	Laboratory of Julio Cordero-Morales	N/A
Plasmid: <i>TRPV1</i> pMO	Laboratory of Julio Cordero-Morales	N/A
Plasmid: <i>GFP</i> pMO	Laboratory of Julio Cordero-Morales	N/A
<i>Trpv6</i> -shRNA	Laboratory of Radhakrishna Rao	N/A
Software and algorithms		
Clampfit 10.4	Molecular Devices	https://www.moleculardevices.com/
Clampex 10.5	Molecular Devices	https://www.moleculardevices.com/
OriginPro 2021	OriginLab	https://www.originlab.com/
Other		
Borosilicate glass	Sutter Instrument	BF150-110-10
Axopatch 200A	Molecular Devices	https://www.moleculardevices.com/
Axon Digidata 1550	Molecular Devices	https://www.moleculardevices.com/

REAGENT or RESOURCE	SOURCE	IDENTIFIER
Individual data deposit	Figshare	[figshare]: [] https://doi.org/10.6084/m9.figshare.13299158x

Author Manuscript

Author Manuscript

Author Manuscript

Author Manuscript